Transformation of valence signaling in a striatopallidal circuit

Donghyung Lee[1], Lillian Liu[1], and Cory M. Root[1]

[1] University of California San Diego, Department of Neurobiology, School of Biological Sciences, San Diego, California

Abstract

The ways in which sensory stimuli acquire motivational valence through association with other stimuli is one of the simplest forms of learning. Though we have identified many brain nuclei that play various roles in reward processing, a significant gap remains in understanding how valence encoding transforms through the layers of sensory processing. To address this gap, we carried out a comparative investigation of the olfactory tubercle (OT), and the ventral pallidum (VP) - 2 connected nuclei of the basal ganglia which have both been implicated in reward processing. First, using anterograde and retrograde tracing, we show that both D1 and D2 neurons of the OT project primarily to the VP and minimally elsewhere. Using 2-photon calcium imaging, we then investigated how the identity of the odor and reward contingency of the odor are differently encoded by neurons in either structure during a classical conditioning paradigm. We find that VP neurons robustly encode reward contingency, but not identity, in low-dimensional space. In contrast, OT neurons primarily encode odor identity in high-dimensional space. Though D1 OT neurons showed larger response vectors to rewarded odors than other odors, we propose this is better interpreted as identity encoding with enhanced contrast rather than as valence encoding. Finally, using a novel conditioning paradigm that decouples reward contingency and licking vigor, we show that both features are encoded by non-overlapping VP neurons. These results provide a novel framework for the striatopallidal circuit in which a high-dimensional encoding of stimulus identity is collapsed onto a low-dimensional encoding of motivational valence.

Introduction

Animals exhibit an impressive ability to change how sensory inputs map onto behavioral outputs. Understanding how animals learn to output different behaviors through experience is one of the fundamental problems in neuroscience. Over the last half century, the field has developed compelling frameworks to tackle this problem at both the algorithmic level (Rescorla-Wagner models, Q-learning models) (Rescorla, 1972; Sutton, 1988) and the mechanistic level (Hebbian learning, STDP, neuromodulation) (Dan and Poo, 2004). By comparison, we lack frameworks through which to understand how the brain might implement learning algorithms through the updating of synaptic weights. One strategy has been to identify neural correlates of latent features assumed to be required for these algorithms (e.g. dopamine as a neural substrate for reward-prediction-error) (Hollerman and Schultz, 1998; Schultz et al., 1997). These results, however, can often be difficult to interpret because reward related signals are found globally throughout the brain (Allen et al., 2019), and are likely multiplexed with signals about motor output and/or stimulus identity. We propose that a more powerful approach is one that compares 1) how the encoding of reward cues changes from one brain nucleus to its downstream target and 2) how much of the encoding can be explained by valence vs. other features such as identity or motor output. In this present work, we implement this comparative approach to the investigation of how encoding of olfactory reward cues is transformed between the olfactory tubercle (OT) and the ventral pallidum (VP) in the context of classical conditioning.

The OT, also known as the tubular striatum (Wesson, 2020), is a 3-layered striatal nucleus situated at the bottom of the forebrain. As with other striatal structures, the OT is composed primarily of Spiny Projection Neurons (SPN's) which express either the *Drd1* or *Drd2* DA receptors (abbreviated as OT_{D1} and OT_{D2}, respectively) (Tritsch and Sabatini, 2012). In addition to receiving a wide range of inputs from cortical and amygdalar areas (e.g. AI, OFC, BLA, PlCoA, Pir) (Zhang et al., 2017b), it receives dense DAergic input from the midbrain (Ikemoto, 2007) and direct input from the mitral and tufted cells of the olfactory bulb (Haberly and Price, 1977; Igarashi et al., 2012; Scott, 1981), a unimodal and primary sensory area. There is a range of experiments that suggest that the OT's DAergic innervation is involved in reward processing. Coincident stimulation of the lateral olfactory tract and DAergic midbrain afferents supports LTP of excitatory current (Wieland et al., 2015) and rats self-administer cocaine, a DAergic drug, into the medial OT more vigorously than to any other striatal nuclei (Ikemoto,

2003). And while the OT neurons are known to respond to a wide range of odorants (Wesson and Wilson, 2010), pairing stimulation of midbrain DAergic neurons with an odor drives appetitive behavior towards the paired odor (Zhang et al., 2017a) and enhances the contrast of the odor-evoked activity (Oettl et al., 2020). Lastly, a number of recent publications report varying degrees of valence signals recorded from neurons in the OT (Gadziola et al., 2020, 2015; Martiros et al., 2022; Millman and Murthy, 2020; Oettl et al., 2020).

The most well-established target of the OT is the VP (Newman and Winans, 1980; Zahm and Heimer, 1987), a pallidal structure that lies immediately dorsal to the OT. In addition to OT input, VP receives strong input from the nucleus accumbens (Jones and Mogenson, 1980) and the subthalamic nucleus (Ricardo, 1980; Turner et al., 2001). More recently, it was reported that VP also receives inputs from several cortical and amygdalar areas that also project to the OT (e.g. Pir, BLA, OFC) (Stephenson-Jones et al., 2020). The VP contains GABAergic neurons, which respond to positive valence cues, and glutamatergic neurons, which respond to negative valence cues. Consistent with their responsiveness, the GABAergic and glutamatergic neurons drive real time place preference and avoidance, respectively (Faget et al., 2018). Though it is well-established that the VP plays a critical role in reward processing, there has been ongoing disagreement on what specific latent features are encoded by VP neurons. Interpretations have included valence (Ottenheimer et al., 2018, 2020b; Richard et al., 2016; Tachibana and Hikosaka, 2012), hedonics (Smith et al., 2009; Tindell et al., 2006), motivation (Faget et al., 2018; Fujimoto et al., 2019; Lederman et al., 2021; Tindell et al., 2005), and reward-prediction error (Ottenheimer et al., 2020a). This ongoing discussion highlights the need to adopt a more comparative approach outlined above.

Here, we investigated the transformation of learned association encoding between the OT and the VP. We began by refining our understanding of OT's efferents to reveal that, contrary to a previous report, both OT_{D1} and OT_{D2} neurons project primarily to the ventrolateral portion of the VP and minimally elsewhere. Given this finding that VP may be the only robust output of the OT, we proposed that the OT to VP circuit is an ideal model system for examining how the encoding of reward cues is transformed between connected brain areas. Comparing the stimulus-evoked activity in OT_{D1}, OT_{D2}, and VP neurons with 2-photon Ca^{2+} imaging, we found that VP neurons encode reward-contingency in low-dimensional space with good generalizability. In contrast, activity in both OT_{D1} and OT_{D2} neurons was high-dimensional and primarily contained information about odor identity, though OT_{D1} neurons are modulated by

83 reward. By examining the same neurons across multiple days of pairing, we propose a putative
84 cellular mechanism for reward-cue responsiveness in VP wherein reward responsive VP
85 neurons gradually become reward-cue responsive. Finally, using a novel classical conditioning
86 paradigm, we provide evidence that non-overlapping sets of VP neurons contain information
87 about the vigor of licking and reward-contingency, but not both.

Results

In order to compare odor-evoked activity in connected brain nuclei, we first characterized which specific subregions of the VP receive input from the anteromedial portion of the OT. While considerable effort has been made to unravel the anatomy and function of the NAc, much less attention has been directed at the OT. Though multiple studies have characterized its anatomical connectivity (Zahm and Heimer, 1987; Zhang et al., 2017b; Zhou et al., 2003), there is inconsistency regarding whether or not OT projects to areas other than the VP. We therefore aimed to clarify previously reported OT connectivity by independently conducting anterograde viral tracing experiments in OT_{D1} and OT_{D2} neurons of the anteromedial OT. To this end, we injected AAVDJ-hSyn-FLEX-mRuby-T2A-syn-eGFP in the anterior OT of *Drd1*-Cre (labels D1+ SPN's) and *Adora2a*-Cre (labels D2+ SPN's) animals (Fig1A, FigS1C-E). Because viral contamination of areas dorsal to the target site can lead to difficulties in interpretation of tracing data, we also injected the same virus to the AcbSh immediately dorsal to the OT for comparison. Consistent with past findings (Kupchik et al., 2015), we observed robust projections VP, LH, and VTA from $AcbSh_{D1}$ neurons and primarily VP projections $AcbSh_{D2}$ neurons (Fig1B-C). We also observed dense labeling of the VP in D1-Cre and A2A-Cre animals injected at the OT. Contrary to one report (Zhang et al., 2017b) but consistent with another (Zhou et al., 2003), we observed minimal labeling in LH and VTA, or anywhere else in the brain, for both OT_{D1} and OT_{D2} experiments (Fig1B-C, FigS1A-B), suggesting that neither OT subpopulation from the anteromedial OT projects strongly outside the VP. As previously reported (Groenewegen and Russchen, 1984). It is also notable that OT projections were restricted to the lateral portions of the VP.

To corroborate and more precisely describe the OT to VP projection, we conducted retrograde tracing by injecting CTB::488 and CTB::543 to the lateral and medial portion of caudal VP, respectively (Fig1D, FigS1F-G). We found strong labeling of soma by both CTB::488 and CTB::543 in the Acb, AI, and Pir (Fig1E-F). By comparison, we found predominantly CTB:488, but not CTB::543, labeling in OT soma, indicating OT neurons are more likely to project to the lateral portion of the VP than to the medial. Similarly, to corroborate the lack of OT to VTA projection, we injected CTB::647 into the VTA (Fig1G, FigS1H-I). Consistent with previous findings (Beier et al., 2015; Faget et al., 2016; Watabe-Uchida et al., 2012), we found dense labeling of soma in various areas of the striatum such as AcbSh, AcbC, and CPu (Fig1H-

119 I). We also found some labeling of soma in some frontal cortical regions such as PrL, AI and IL
120 cortices. In contrast, we found that hardly any OT neurons were labeled. The rare OT neurons
121 that did have CTB labeling were exclusively localized to the dorsal most portion of layer III,
122 closely bordering the VP. Taken together, we conclude that both D1 and D2 SPN's of the
123 anteromedial OT project primarily to the lateral portion of the VP and negligibly to other brain
124 areas, including the VTA.

125 Once we had identified that OT has extremely constrained outputs to the lateral VP, we
126 set out to comparatively characterize the encoding of reward cue in this striatopallidal circuit.
127 Past analysis of valence encoding is confounded by not accounting for the difficult-to-avoid
128 overlaps among identity, salience, and reward contingency. To address this, we carefully
129 designed a 6-odor conditioning paradigm where these factors could be decoupled (Fig2A).
130 During each trial, the animal is exposed to 1 of 6 odors for 2 seconds. At the end of odor
131 delivery, the animal either receives: 2 µl of a 10% sucrose solution (S), 50 ms of airpuff at 70 psi
132 (P) or nothing (X). 3 of the odors are ketones (hexanone, heptanone, octanone) and the rest are
133 terpenes (terpinene, pinene, limonene), but the pairing contingencies are chosen such that each
134 contingency group (S, P, or X) includes 1 ketone and 1 terpene. We reason that in a valence-
135 encoding population, but not in an identity-encoding population, we should see that odor pairs of
136 different reward-contingency (e.g. S_K, a sucrose-paired ketone vs. P_K, an airpuff-paired ketone)
137 are more different than odor pairs of same reward-contingency (e.g. S_K, a sucrose-paired
138 ketone vs. S_T, a sucrose-paired terpene). Additionally, because both sucrose-pairing and
139 airpuff-pairing should make the associated odor more salient, we can disambiguate between
140 increased discriminability due to salience vs. valence by comparing neural activity in response
141 to sucrose-cues or airpuff-cues.

142 To record the activity of the OT and VP neurons across multiple days of pairing, we
143 injected C57BL/6 mice with AAV9-hSyn-jGCaMP7s-WPRE (lateral VP) and *Drd1*-Cre or
144 *Adora2a*-Cre animals with AAV9-hSyn-FLEX-jGCaMP7s-WPRE (anteromedial OT) (Fig2B,
145 FigS2A-F). Additionally, we implanted a 600µm Gradient Refractive Index (GRIN) lens 150µm
146 dorsal to the virus injection site and cemented a head-fixation plate to the skull. 6-8 weeks after
147 surgery, animals were water-restricted and habituated for 3-5 days in the head-fixation setup
148 (Fig2C). We processed the acquired time-series images using Constrained Nonnegative Matrix
149 Factorization (Pnevmatikakis et al., 2016) to obtain fluorescence traces from each putative
150 neuron (Fig2D,E). In total, we recorded Ca^{2+} signals from 231 OT_{D2} neurons from 6 *Adora2a*-

151 Cre animals (FigS3), 288 OT_{D1} neurons from 6 *Drd1*-Cre animals (FigS4) and 130 VP neurons
152 from 5 C57BL6/J animals (FigS5).
153 After 3 days of odor-sucrose associations, the animals displayed anticipatory licking
154 behavior primarily during sucrose-paired odors (Fig2F,G). Starting on day 4, the sucrose and
155 airpuff contingencies were switched such that every odor had a reassigned contingency. By day
156 6, animals had adapted their anticipatory licking behavior to match the new sucrose-contingency
157 (Fig2G). Quantification of the animal's licking behavior showed that the accuracy of animals'
158 licks during odor increased across time and was not different across lens-placement groups
159 (Fig2H, TableS4,S5; ANOVA: F_{day}=27.64, p_{day}=2.29e-16, $F_{lens\ location}$=2.30, $p_{lens\ location}$=0.11).
160 These results show that the animals learn to associate S odors with reward in a flexible manner
161 in our paradigm. Because we saw the strongest behavioral evidence that animals learned odor-
162 sucrose associations by day 6, we focused our analysis on how reward cues are encoded on
163 the last day of imaging. The animals also showed trends of behavioral changes in response to
164 airpuff-cues, though they were not significant: during airpuff-cues, animals walked less and
165 closed their eyes more than during other odors (FigS6D-G, TableS32-S36). These behavioral
166 changes for aversive cues were less robust than that for reward association. However, animals
167 show clear responses to the US indicating that they perceive the aversive stimulus.
168 OT and VP neurons showed heterogeneous responses to 6 odors across all 6 days of
169 imaging (FigS3, FigS4, FigS5). To unbiasedly describe the difference between regions, we
170 performed hierarchical clustering on the pooled trial-averaged responses to the 6 odors on the
171 6th day of imaging (Fig3A). We observed both inhibitory (clusters I, II) and excitatory (clusters
172 III-VI) responses to odors as well as broad (clusters II, VI) and narrow (clusters IV, V) odor-
173 tuning (Fig3B). Cluster I and cluster III most closely fit our description of putative valence-
174 encoding neurons, i.e. neurons that had similar responses to 2 sucrose-cues (S_K vs. S_T) but
175 different responses to a sucrose-cue and a puff-cue or control odor (S_K vs. P_K or X_K). Although
176 all clusters included neurons from all subpopulations, cluster I and cluster III, which showed
177 larger responses to odors predicting sucrose, were enriched for VP neurons (Fig3C), leading us
178 to hypothesize that individual neurons in the VP were more likely to be valence encoding
179 neurons than in either OT subpopulation.
180 To assess this hypothesis, we quantified the number of neurons that had statistically
181 significant responses to each of the 6 odors on the last day of imaging. We found that more VP
182 neurons were either excited (29.8±4.1%, 36.6±4.0% for S_K, S_T) or inhibited (24.5±3.0%,

183 29.4±3.8% for S_K, S_T) to either sucrose-paired odor than to control or puff-paired odors (7.6-
184 11.1% excited, 8.1-12.9% inhibited) (Fig3D, FigS8A-B, TableS37). When compared across
185 days, we found that the percentage of VP neurons that respond to both S odors increases from
186 6.1±2.2% on day 1 to 34.1±5.1% by the 6th day of imaging (Fig3E,TableS11). By comparison,
187 the percentage of OT neurons that respond to both S odors in the same direction (i.e. excited by
188 both S odors or inhibited by both S odors) did not increase through training. Furthermore,
189 whereas OT_{D1} and OT_{D2} neurons were more likely to respond to a single odor than they were to
190 respond to both S odors (12.6 vs 31.3% in OT_{D1}, 11.8 vs 21.7% in OT_{D2}), VP neurons were
191 more likely to respond to both S odors than to a single odor (34.1 vs 23.3%).
192 Similarly, we found that the magnitude of trial-averaged odor responses in the VP were
193 significantly higher for S odors than X or P odors on the last day of imaging (FigS9, TableS38).
194 By comparison, neither sucrose-pairing nor airpuff-pairing had any impact on the magnitude of
195 odor responses in OT_{D2} neurons on day 6. And though we did observe a significant effect of
196 sucrose-pairing on response magnitudes in OT_{D1} neurons, both the effect size and significance
197 were weaker than observed in VP. We propose that an ideal valence-encoding neuron should
198 respond similarly to 2 odors of equal reward-contingency but disparate molecular structure, and
199 we looked at the correlation between each neuron's response to the sucrose-paired ketone (S_K)
200 and to the sucrose-paired terpene (S_T). VP neurons had a high correlation between a neuron's
201 responses to S_K and S_T (Fig3F; R^2=0.89). This similarity was much higher than between the
202 sucrose-paired ketone (S_K) and the control ketone (X_K) despite the greater structural similarity
203 between S_K and X_K (Fig3G; R^2=0.33). In contrast, for both OT_{D1} and OT_{D2} neurons, there was a
204 higher correlation between responses to similar molecular structure (S_k and $X_{K,}$) than between
205 responses to similar contingency (S_K and S_T) (OT_{D2}: S_K vs. S_T R^2=0.04, S_K vs. X_K R^2=0.58; OT_{D1}:
206 S_K vs. S_T R^2=0.13, S_K vs. X_K R^2=0.40). Moreover, most VP neurons (76.5%), had a smaller
207 absolute difference in the response magnitude to the 2 S odors ($|S_K-S_T|$) than the absolute
208 difference between the sucrose-paired ketone and the control ketone ($|S_K-X_K|$) (Fig3H). By
209 comparison, only half of OT_{D2} and OT_{D1} neurons showed smaller $|S_K-S_T|$ than $|S_K-X_K|$, as would
210 be expected if response magnitude to an odor did not depend on reward-contingency. This
211 trend was not due to the fact that VP neurons were more likely to respond to both S odors than
212 OT neurons were since it was consistent across various thresholds for odor response
213 magnitude. This trend was consistent for other pairwise odor comparisons where one odor was
214 a sucrose-cue and the other was not (e.g. S_K vs. P_T, FigS10A-B).

215 Finally, we reasoned that the activity of reward-contingency encoding neurons would
216 support good decoding of odor pairs which have different valence but not of odor pairs that have
217 the same valence. To do this, we trained binary logistic classifiers from each neuron's response
218 to all 15 odor pairs and quantified the area under their receiver operating characteristic
219 (auROC). Because auROC values were non-normal with large spread, we quantified what
220 percentage of neurons had an auROC of at least 0.75, halfway between ideal and at-chance
221 decoding. We also note that all classifiers with auROC>0.75 showed bootstrapped p-values less
222 than 10^{-3} (FigS10C-D). To assess whether neurons from each region were encoding valence,
223 we compared a neuron's {S_K vs. X_K} decoder performance (*inter*valence classification) against
224 its {S_K vs. S_T} decoder performance (*intra*valence classification) (Fig3I-K, FigS10E-F). Across
225 multiple days of imaging, we found that the percentage of neurons that support intervalence
226 classification increased regardless of region but that this effect was markedly more pronounced
227 among VP neurons than among OT_{D1} or OT_{D2} neurons (Fig3I-J, TableS12-S15, FigS10F,
228 TableS39-S41). Intravalence classification, however, did not depend on days or region (Fig3K,
229 TableS16-S17, FigS10F, TableS42-S44). By day 6, there were thrice as many VP neurons with
230 good intervalence decoding than with intravalence decoding (51.8±5.0% vs. 14.4±5.8% for {S_K
231 vs X_K} and {S_K vs S_T}, respectively). In contrast, a similar number of OT neurons displayed good
232 intervalence decoding as did intravalence decoding (20.8% vs 19.9% of OT_{D1}; 12.8% and
233 21.0% of OT_{D2} for {S_K vs X_K} and {S_K vs S_T}, respectively). The pattern of better intervalence
234 decoding than intravalence decoding among VP neurons was observed across all 15 pairwise
235 classifiers (FigS10H). Whereas 10.2% of all day 6 VP neurons had auROC>0.75 for {S_K vs. S_T},
236 46.9-57.8% had auROC>0.75 for any classification between a sucrose-cue and a control odor
237 or airpuff-cue. By comparison, there were few neurons with auROC>0.75 for any classification
238 between a puff-cue and a control odor (2.3-10.9%), suggesting that negative valence is either
239 not encoded in these VP neurons or the negative valence was not learned.
240 Plotting a neuron's {S_K vs. S_T} auROC against its {S_K vs. X_K} auROC, we can categorize
241 a neuron into the 4 categories (Fig3L). 1) a valence encoding neuron ({S_K vs. S_T}<0.75 and {S_K
242 vs. X_K}>0.75), 2) an identity encoding neuron (both auROC>0.75), 3) an identity encoding
243 neuron that does better with S odors ({S_K vs. S_T}>0.75 and {S_K vs. X_K}<0.75), and 4) an
244 uninformative neuron (both auROC<0.75). According to this categorization, half of VP neurons
245 were valence encoding by day 6, followed by OT_{D1} then OT_{D2} (Fig3M-N; 47.7, 16.2, 7.3% for
246 VP, OT_{D1}, and OT_{D2}, respectively). The opposite was true for identity encoding. VP had a

247 smaller percentage of identity encoding neurons than either OT_{D1} or OT_{D2} (14.8, 21.1, 22.9% for
248 VP, OT_{D1}, and OT_{D2}, respectively). We note that these conclusions can also be replicated when
249 analyzing multinomial regression (MNR) classifiers trained on single neuron activities (FigS11F-
250 G, TableS50-S53). Namely, the rates of confusion between the 2 sucrose cues are highest in
251 VP and lowest in OT_{D2} whereas the rates of confusion across all ketones (S_K, X_K, P_K) are
252 highest in OT_{D2} and lowest in VP. These single-neuron classifier analyses further indicate that
253 VP neurons, more than either OT_{D2} or OT_{D1} neurons, were encoding reward contingency at the
254 single neuron level. However, the most striking observation was that while only a subset
255 (37.5%) of VP neurons had auROC<0.75 for both {S_K vs. X_K} and {S_K vs. X_K}, a majority of OT_{D2}
256 and OT_{D1} neurons (69.7% and 62.6%, respectively) showed auROC<0.75 for both {S_K vs. S_T} or
257 {S_K vs. P_K}. Thus, in comparison to the VP, most individual OT neurons have little discriminatory
258 information about olfactory stimuli regardless of valence at the single-neuron level and may be
259 better suited in a population code.
260 Our data indicated that valence encoding emerges in VP neurons over the course of
261 learning. To explore the potential mechanisms at the cellular level, we compared the activity of a
262 subset of neurons we could observe on both day 1 and day 3 (Fig4A-F). We noticed there were
263 neurons that responded to the sucrose delivery on day 1 that responded to the sucrose cue on
264 day 3 (Fig4C,F), reminiscent of models of Hebbian plasticity. When quantified, we found that
265 17.9, 20.9% of VP neurons were responsive to sucrose on day 1 and S_K and S_T on day 3,
266 respectively (Fig4G). We specifically considered neurons that had the same direction of
267 response (excitation or inhibition) to both cues on separate days. This figure was much lower
268 among OT subpopulations (11.5, 8.2% for S_K and S_T in OT_{D1}; 10, 2.5% for S_K and S_T in OT_{D2}).
269 Consistent with above observations, we also found that the odor responses to sucrose-cues
270 were larger on day 3 than day 1 in 85% of tracked VP neurons, but only in 65% and 57% of
271 OT_{D1} and OT_{D2} neurons, respectively (Fig4H-I, TableS18-S19). We did not see the same effect
272 in VP neurons' responses to control or puff-paired odors. Together, our data suggest that
273 sucrose pairing causes sucrose-responsive VP neurons to increase their responses to the
274 sucrose-predictive odors.
275 Olfactory brain areas are known to use population codes to encode sensory information,
276 whereby single neurons have weak discriminatory information, but the activity of the population
277 allows for an efficient encoding of high-dimensional data. To assess if there is discriminatory
278 information about the odorants within the population-level activity, we compared the pairwise

Euclidean distance of trial-averaged odor responses for all 15 odor pairs (Fig5A,B). We saw that, in general, the pairwise Euclidean distance for all odor pairs examined increases quickly after the onset of odor, reaches peak distance towards the end of the 2 second odor delivery, and slowly decays after odor ends (Fig5A). When examining the average pairwise distance during the last second of odor, there was a relatively unstructured distribution of pairwise distance in OT_{D2} odor-response such that $||S_K-X_K||$, $||S_K-P_K||$, $||S_K-S_T||$, and $||X_K-X_T||$ were all similar (Fig5B). By comparison, in VP populations, the distribution was structured such that intervalence pairwise comparisons between sucrose-paired and not sucrose-paired odors (e.g. $||S_K-P_K||$ and $||S_K-X_K||$) were larger than intravalence pairwise comparisons (e.g. $||S_K-S_T||$, or $||X_K-X_T||$). OT_{D1} populations showed an intermediate trend where most intravalence pairwise distances were smaller than intervalence pairwise distances with the exception of $||S_K-S_T||$. Thus, at the population level VP representations appear to encode valence but not identity, whereas OT representations encode some valence information but appear to be better suited for identity encoding.

In parallel, we also performed decoding analysis using linear classifiers to assess how reliably a given pair of odors could be decoded from population-level activity (Fig5C-D). To quantify this, we extracted the average $\Delta F_{i,k}/F$ values for each trial $i \in [1,m]$ and each neuron $k \in [1,n]$. The resulting matrix of size m x n was used to train a binary linear classifier with a logistic learner. For each classifier, we looked at the average accuracy across 5-fold cross-validation (CV accuracy). Classifiers were trained on simultaneously recorded populations (i.e. neurons from the same animal recorded on the same day) to capture biological variability. A total of 765 pairwise linear classifiers were trained (15 pairwise comparisons, 17 animals, and 3 days). When compared against 10,000 shuffles, 569 of these classifiers showed bootstrapped p-value less than 0.001 (FigS12A). Importantly, all classifiers with CV accuracy higher than 0.75 had p-value less than 0.001.

Linear classifiers trained on day 6 OT_{D2} population data had similar ranges of accuracy regardless of valence (Fig5D). For example, the intravalence classification $\{S_K$ vs. $S_T\}$ was more accurate (86.6±3.9**%**) than some and intervalence classifications (e.g. $\{S_K$ vs. $X_K\}$, 72.8±5.4**%**) but less accurate than others (e.g. $\{S_T$ vs. $P_K\}$, 88.2±3.1**%**). Classifiers trained on VP population activity, however, always showed more accurate intervalence decoding (range: 89.5-96.1%) than intravalence decoding ($\{S_K$ vs. $S_T\}$, 79.9±6.1**%)**. Additionally, whereas OT_{D2} population classifiers could decode the 2 control cues $\{X_K$ vs. $X_T\}$ at accuracy (85.8±4.2**%)** comparable to

311 sucrose-cue vs. non-sucrose-cue, VP population classifiers were consistently less accurate
312 (76.8±3.7**%)** at {X_K vs. X_T} than the aforementioned intervalence classifiers. This suggests that
313 whereas OT_{D2} encodes odor identity agnostic to the valence, VP does not encode identity at all
314 but rather encodes reward contingency or positive valence. OT_{D1} pairwise classification was a
315 mixture of the other 2 regions: sucrose-cue vs. non-sucrose-cue classification was more
316 accurate than most other pairwise classifications (range: 86.4-94.3%), but the {S_K vs. S_T}
317 classification was comparably accurate (90.9±4.7%). This rules out the interpretation that OT_{D1}
318 strictly encodes valence since the identity of 2 sucrose-cues can be decoded well.
319 To address the possibility that our results are due to the limitations of linear
320 classification, we repeated the analysis using support vector machines (SVM's) with a radial
321 basis function kernel and found we could draw the same conclusions (FigS12E). Similarly, to
322 verify our results are not epiphenomena of forcing the data into binary classification, we looked
323 at population-level MNR classifiers trained on day 6 data. Importantly, we observe high
324 confusion between 2 sucrose cues in MNR classifiers trained on VP data, but not those trained
325 on OT_{D2} or OT_{D1} data (FigS12F), corroborating through an alternate analysis method that VP
326 population activity encodes reward contingency whereas either OT subpopulations are better at
327 encoding identity.
328 The fact that VP populations showed higher decoding for odor pairs of unequal sucrose-
329 contingency provides strong evidence that VP encodes reward-contingency more than identity.
330 Results from OT decoder analyses, however, are less intelligible: all 15 odor pairs, regardless of
331 sucrose-contingency, could be decoded with above-chance success. Though this result is
332 consistent with OT populations encoding identity rather than valence, it does not rule out the
333 possibility that valence and identity are both encoded. In the context of cue-association, 2 cues
334 of different valence cannot have the same identity, meaning that good decoding of {S_K vs. P_K}
335 can be extracted from either valence encoding or identity encoding populations. To
336 disambiguate these 2 possibilities, we looked at the generalizability of pairwise decoders.
337 Briefly, linear classifiers were trained on each of the 15 possible odor pairs. Afterwards, the
338 resulting classifier was tested on every other odor pair (Fig5E). We reasoned that if neural
339 populations encode valence in addition to identity, classifiers trained on any odor pair of unequal
340 sucrose-contingency should consistently perform above chance on a different odor pair of
341 unequal sucrose-contingency (e.g. train on {S_K vs. P_K}, test on {S_T vs. X_T}). In other words, given
342 valence encoding, {S_K vs. P_K} should be discriminable in a way that can also discriminate {S_T vs.

343 X_T}. As expected, VP population decoders were consistently generalizable when trained on odor
344 pairs of unequal sucrose-contingency then tested on other odor pairs of unequal sucrose-
345 contingency (Fig5F,G). OT_{D2} population decoders, on the other hand, showed negligible
346 generalizability across pairs of unequal sucrose-contingency. Similarly to other metrics of
347 valence encoding, we found that OT_{D1} displayed a generalizability in between that of VP and
348 OT_{D1}, suggesting that OT_{D1} could encode some valence in addition to identity. However, we
349 note that the VP population, on average, outperforms OT_{D1} at generalized valence decoding
350 (95.0±2.0**%** vs 78.5±3.9**%;** TableS22-S23).
351 After performing these population-level analyses, we noticed a discrepancy: although
352 single-neuron intervalence decoding was worse in OT than in VP (Fig3M-N), population-level
353 intervalence decoding was comparable between either OT subpopulations and the VP (Fig5C-
354 D). This led us to speculate that the encoding of odor information had a higher dimensionality in
355 OT than in VP. To explicitly compare the dimensionality of VP and OT population activities, we
356 looked at the extent to which the population vector is spread across multiple axes using
357 principal component analysis (PCA). Dimensionality can further be quantified using the
358 participation ratio (PR) of a population, which is the square of the sum of eigenvalues of its
359 covariance matrix divided by the sum of the squares of its eigenvalues (Litwin-Kumar et al.,
360 2017; Recanatesi et al., 2019). This value will have a range of 1 to n, where n is the total
361 number of features. If a single principal component can describe all of the total population
362 variance (i.e. the data is low-dimensional), the population will have PR equal to 1. Conversely, if
363 every principal component equally describes n^{th} of the total variance (i.e. the data is high-
364 dimensional), the population will have PR equal to n. Because the number of total neurons
365 recorded was different between OT and VP experiments, we first assessed if and how the
366 normalized PR would vary with the number of total neurons through random sampling (Fig5H).
367 After observing a consistent decrease in PR with increasing n, we compared the PR of OT and
368 VP animals by repeatedly subsampling a fixed number of neurons (k=15) and found that VP
369 animals had lower PR (PR_{VP} =5.83±0.80) than either OT_{D2} (PR_{D2}=9.61±0.37) or OT_{D1}
370 (PR_{D1}=9.24±0.44) animals after training (Fig5I, TableS24-S25). There was also a difference,
371 however, in how valence information vs. identity information was encoded by VP populations.
372 Though the first PC of each VP population was sufficient to train adequate {S_K vs. P_K} decoders
373 (CV $accuracy_{PC1}$ = 85.5±2.7%), all 15 PC's were required for comparable {S_K vs. S_T} decoding
374 (CV $accuracy_{PC1:15}$ = 75.1±13.4%) (Fig5J-L, TableS26-S29). In either OT populations, the first

375 PC did not support good decoding of either {S_K vs. P_K} or {S_K vs. S_T}. Together, our population-
376 level analysis indicates that VP encodes valence, but not identity, in low-dimensional space,
377 OT_{D2} encodes identity but not valence in high-dimensional space, and OT_{D1}, has some valence
378 information and encodes identity in high-dimensional space.
379 Analyses at the single-neuron and population levels showed that VP activity encodes
380 reward contingency, rather than the identity, of the olfactory stimulus. However, due to the task
381 design, the reward-contingency of a stimulus was highly correlated with the vigor of licking
382 (Fig2F). This raised concerns that some neurons classified as robust reward-contingency
383 encoders were potentially encoding motor-related information. Indeed, many VP neurons
384 showed consistent increases in fluorescence time-locked to the onset of a licking-bout
385 (FigS13A-B), and could be used to train distributed lag models to predict onset of licking bouts
386 (FigS13C). Across all VP neurons, we observed a positive and significant correlation between a
387 neuron's valence decoding ability and licking decoding ability (FigS13D; slope=0.41, $p=2.2\times10^{-}$
388 ^{10}, R^2=0.28). This motivated us to develop a new conditioning paradigm that could decouple
389 reward-contingency of an odor cue from the behavioral output.
390 Initially, we attempted to train animals on a symmetric Go/No-Go operant task where
391 reward delivery was contingent on licking or withholding licks during odor. However, consistent
392 with previous findings (Gubner et al., 2010), we found that animals struggled to learn the No-Go
393 behavior in comparison to the Go behavior (data not shown). In an operant paradigm, this leads
394 to a problematic difference in valence of Go/No-Go cues. Consequently, we opted to develop a
395 classical conditioning paradigm whereby licks were encouraged/discouraged by physically
396 moving the lick spout before odor presentation (Fig6A-B).
397 Briefly, headfixed animals were presented with 1 of 6 odors in pseudorandomized order.
398 During the presentation of 3 of these odors, the lick spout was moved away from the mouse
399 with a linear stepper motor. These odors are denoted as N odors (N for No-lick spout). During
400 the presentation of the other 3 odors, the lick spout remained within licking distance of the
401 mouse's tongue. These odors are referred to as L odors (L for lick spout). 1 odor from each
402 group served as a control odor that had 0% reward-contingency (L_X, N_X). The other 2 odors in
403 each group were paired with sucrose at low (50%) or high (100%) probability (L_{lo}, L_{hi}, N_{lo}, N_{hi}).
404 We reasoned that this contingency could allow us to make pairwise comparisons where one
405 odor has a higher value but lower anticipatory licking than the other (e.g. N_{hi} vs. L_{lo}).

406 To monitor anticipatory licking in the absence of the lick spout, we trained a distributed lag
407 model (DLM) using features of the mouse's face tracked using DeepLabcut (Mathis et al., 2018)
408 (FigS13E-G). We chose to pool data across all mice from the day of the highest licking
409 differential between L_{hi} and N_{hi} odors (FigS13H) to maximize the decoupling of value and motor
410 output in our analysis. Anticipatory licking during L_{lo} or L_{hi} began during the last second of the
411 odor and increased gradually until sucrose delivery whereas licking during N_{lo} or N_{hi} was
412 delayed by about one second (Fig6C). When quantified across animals on their days of highest
413 lick differential, we found that mice consistently licked most during L_{hi}, followed by L_{lo} and N_{hi},
414 then N_{lo} (Fig6D, TableS30-S31). Mice showed little to no licking during either control odors.
415 Thus, this behavioral assay affords us the opportunity to assess the decoupled effects of
416 reward-contingency and licking vigor on neural activity.
417 To begin to characterize the presence of reward-contingency and/or licking vigor
418 encoding in the VP, we first pooled and clustered the neural activity taken from 5 animals on
419 their days of highest lick-differential (Fig6E). When clustering VP neurons into 3 clusters, we
420 found that one cluster (I) showed a largely similar inhibitory response to the 4 sucrose-paired
421 odors, but not control odors- much like cluster (I) from the previous conditioning experiment
422 (Fig3A-B, Fig6E-F). Another cluster (III) by comparison, showed a varied excitatory response to
423 each of the 4 sucrose-paired odors, much like cluster III from the previous experiment. Cluster
424 (III) neurons seemed to have a particularly strong response to L_{hi} for which there was most
425 anticipatory licking. This led us to speculate the existence of both reward-contingency encoding
426 and vigor encoding neurons in the VP.
427 To test this directly, we quantified single neuron decodability of odor pairs and examined
428 how correlated decoding along the reward-contingency axis is to decoding along vigor axis
429 (Fig6G-H). We reasoned that auROC values for {L_{hi} vs. N_{hi}} would be high for vigor encoding
430 neurons but not value encoding neurons given these 2 odors have the same reward-
431 contingency but disparate licking behaviors. Similarly, we reasoned that auROC values for {N_{hi}
432 vs. N_X} would be high for reward-contingency encoding neurons but not vigor encoding neurons
433 given there is a large difference in value but small difference in licking between these 2 odors.
434 First, we saw that while single neuron decodability along the reward-contingency axis (e.g. {N_{hi}
435 vs N_X}) was higher than along the lick axis (e.g. {L_{hi} vs N_{hi}}), there were more neurons that could
436 decode {N_{hi} vs N_X} than could decode {L_X vs N_X} at auROC>0.75 (Fig6G-H). Furthermore, we
437 saw a lack of significant correlation between the single-neuron decodability of 2 odors that had

438 similar licking but different reward-contingency ({N_{hi} vs N_X}) and the decodability of 2 odors that
439 had different licking but same reward-contingency ({L_{hi} vs. N_{hi}}) (Fig6I; slope=0.038, p=0.61,
440 R^2=0.0039). This decoupling suggests that reward-contingency and vigor information are both
441 encoded in the VP but by different populations. As a control, we saw a significant correlation
442 between 2 pairwise comparisons that both had high difference in reward-contingency ({N_{hi} vs
443 N_X} and {L_{hi} vs L_X}) (Fig6J; slope=0.60, p=3.8×10^{-10}, R^2=0.30).
444 We also performed the converse experiment where the $\Delta\Delta F/F_{baseline}$ values of each
445 neuron were linearly fitted to either 1) the reward contingency, 2) the anticipatory licking or 3)
446 both values and the interaction term. Then, we compared the ΔR^2 when either variable was
447 omitted in the model and plotted the $\Delta R^2_{\text{-valence}}$ against the $\Delta R^2_{\text{-licking}}$ (Fig6K). We reasoned that,
448 if a typical VP neuron's activity could be well-explained by either reward-contingency or vigor
449 but not both, we would see points along either x or y-intercepts. On the other hand, if a typical
450 neuron's activity could be well-explained by a linear combination of the 2 variables, we would
451 see data fall along a line of positive slope. We found that most neurons tended to have large
452 $\Delta R^2_{\text{-valence}}$ *or* large $\Delta R^2_{\text{-licking}}$ values but not both, supporting the idea that 2 largely non-
453 overlapping sets of VP neurons encode reward-contingency *or* vigor but not both.
454 Lastly, we trained linear classifiers of pairwise odor comparisons using population-level
455 activity to assess if both reward-contingency and vigor information were present in the
456 population-level activity. Consistent with single-neuron decoder analysis, we found that {L_{hi} vs
457 L_X} and {N_{hi} vs N_X} could both be decoded better than {L_X vs N_X} (Fig6L-M). Because we train
458 each classifier using simultaneously recorded neural activity (i.e. from a single animal), we had
459 a total of 75 classifiers (15 pairwise classifiers for 5 animals). The cross validated accuracies of
460 these classifiers were then fitted to a linear model of pairwise differences in either 1) reward-
461 contingency, 2) anticipatory licking, or 3) both. If the population VP activity encodes either
462 reward-contingency or vigor but not both, we expect to see one of the single-variable models
463 outperform the other greatly. But if the population VP activity encodes both variables, we expect
464 the multivariable model would outperform either single model. We found that Δlicking has a
465 weak and not significant relationship with pairwise CV accuracy (Fig6N; slope=0.076, p=0.079,
466 R^2=0.042). By comparison Δreward-contingency (or P(S), as in probability of sucrose delivery
467 following odor) had a larger and statistically significant correlation with pairwise accuracy
468 (Fig6O; slope=0.15, p=3.7×10^{-4}, R^2=0.16). The combined model, however, showed larger
469 coefficients and larger R^2 than either single variable model, suggesting an additive effect of both

470 features on CV accuracy (Fig6P; accuracy = 0.18Δlick + 0.24ΔP(S) - 0.22Δlick*ΔP(S) +0.65,
471 R^2=0.23). Thus, we conclude that both reward-contingency and licking vigor are encoded in the
472 population-level activity of VP neurons.

473

Discussion

Our anatomical investigations demonstrate that the primary output of the OT is to the VP, with minimal connections to the VTA. Given its constrained connectivity, we propose that the OT to VP circuit is an ideal model system for examining how the encoding of reward cues is transformed across brain circuits. Utilizing comparative longitudinal imaging, we found that VP, but not OT_{D2}, robustly encodes the sucrose-contingency of odors. Although our analyses revealed that sucrose-contingency influences odor-evoked responses in OT_{D1} neurons more so than in OT_{D2} neurons, other evidence suggests valence encoding is not the appropriate framework for interpreting OT_{D1} activity. Specifically, information about sucrose-contingency in OT_{D1} resides in a high-dimensional space and generalizes poorly, whereas VP encodes reward-contingency robustly in a low-dimensional and generalizable manner. Thus, we suggest that the changes in OT_{D1} activity are more likely to reflect increased contrast of identity or an intermediate and multiplexed encoding of valence and identity. Finally, using a novel classical conditioning paradigm, we assigned motor-related signals and expected-value signals to non-overlapping VP subpopulations.

Some of our findings were unexpected. For example, we found no evidence that either OT_{D1} or OT_{D2} have significant extrapallidal outputs. This is in contrast to a previous study which reported that OT_{D1} neurons, and to a lesser extent, OT_{D2} neurons, project to the LH and VTA (Zhang et al., 2017b). It is possible that other parts of the OT have extrapallidal outputs, as we only performed anterograde tracing from the anteromedial portion. It is also possible that at least some of the VTA labeling Zhang and colleagues observed from anterograde viral tracing experiments could be due to backflow of the tracer virus in nuclei immediately dorsal to the OT (e.g. AcbSh). As a critical control, we provide evidence that retrograde tracing from VTA robustly labels AcbSh neurons but hardly any OT neurons. And the few VTA projecting OT neurons we did observe were restricted to the distal portions of layer III bordering the VP. Consistent with this, quantification of OT afferents is glaringly absent from 2 independent characterizations of brainwide inputs onto VTA (Beier et al., 2015; Faget et al., 2016). In contrast, OT has been reported to be one of the most prominent inputs to both GAD2+ and Vglut2+ VP neurons (Stephenson-Jones et al., 2020). It is difficult, however, to completely rule out the existence of OT *to* midbrain projections due to the limitations of our experiments: we primarily targeted layer II in the anteromedial portion of the OT for anterograde tracing and only

505 tested the VTA with retrograde tracers. More posterior and/or lateral portions of the OT could
506 have extrapallidal outputs posterior to the VTA. Despite these caveats, the evidence suggests
507 that *Drd1*+ neurons in the anteromedial portion of the OT have little extrapallidal projections
508 when compared to the AcbSh.

509 Though we found little difference in the output patterns of OT_{D1} and OT_{D2} neurons, we
510 observed differences in how these 2 subpopulations encode odor valence. Consistent with a
511 previous report (Martiros et al., 2022), we found that OT_{D1} activity, more than OT_{D2} activity, is
512 modulated by reward contingency. For example, OT_{D1} neurons, but not OT_{D2} neurons, were
513 more likely to respond to sucrose-paired odors than other odors. And the magnitude of
514 responses in OT_{D1} but not OT_{D2} neurons were significantly larger to sucrose-paired odors than
515 to other odors. We refrain, however, from concluding that the primary feature encoded in OT_{D1}
516 neurons is valence or reward contingency, for the following reasons. First, the above-mentioned
517 effects of sucrose-contingency on neural activity are much stronger for VP than for OT_{D1}.
518 Additionally, whereas more than 50% of VP neurons could be categorized as reward-
519 contingency encoders, this figure was less than 20% for OT_{D1}. Lastly, population-level decoders
520 trained on odor pairs of different valence can generalize in the case of VP populations, but not
521 OT_{D1} populations. While we acknowledge that there is poor standardization when it comes to
522 defining valence encoding, it is unlikely that discrepancies between our conclusions and those
523 of Martiros et al. stem from differences in interpretation alone. Comparative examination of our
524 analyses reveals clear dissimilarities in the effect-size of shared metrics (e.g. % odor
525 responsive). Given the high Z-resolution afforded by 2-photon microscopy, it is probable that we
526 recorded from different layers of the OT, which should not be assumed to have identical
527 physiology. We note that the lens placements in our experiments are considerably more ventral
528 than those reported in Martiros et al. It is possible that these neurons are recorded from layer III
529 of the OT whereas the majority of the neurons in the present study are recorded from layer II. A
530 direct comparison of layer II and layer III OT neurons and their valence encoding could prove
531 useful in understanding the discrepancies between the two studies. It is also possible that some
532 of the neurons recorded in Martiros et al. could be from the rostral portion of the VP which lies
533 immediately dorsal to layer III of the OT. Although *Adora2a* and *Drd1* are not expressed as
534 mRNA in the VP, the BAC-transgenic lines used for both the present work and work by Martiros
535 et al. labels neurons in the VP.

536 Our comparison of OT and VP is reminiscent of previous comparisons made between
537 value encoding in VP and NAc (Ottenheimer et al., 2018; Richard et al., 2016). These
538 publications showed that VP encodes incentive value more robustly than the NAc. Given that
539 OT and NAc share many anatomical, physiological, and molecular traits, it is tempting to
540 speculate that the encoding schemes, too, would be similar between the 2 areas. Optogenetic
541 activation of OT_{D1} supports RTPP (Murata et al., 2019), as does activation of D1 or D2 neurons
542 of the NAc (Soares-Cunha et al., 2020). While we acknowledge stimulation experiments provide
543 unique insights that cannot be obtained from recordings alone, we note that SPN's have
544 extensive inhibitory collaterals and exhibit high-dimensional activity. Given these peculiarities of
545 the striatum, we predict that bulk stimulation leads to activity patterns well outside the
546 physiologically relevant range and that this warrants conservative extrapolations regarding OT
547 SPN's endogenous role.
548 An exciting conclusion from our work is that, within the context of our conditioning
549 paradigm, the dimensionality of neural activity was much lower in VP than in OT. Furthermore,
550 the dimensionality of the imaged subpopulations were anti-correlated with the robustness of
551 sucrose-contingency encoding: OT_{D2} displayed the highest dimensionality and lowest valence
552 encoding whereas VP displayed the lowest dimensionality and highest valence encoding. As
553 discussed elegantly by others (Chu et al., 2016; Shannon, 1948), there is generally a tradeoff
554 between the efficiency of a neural population (i.e. its total information capacity) and the
555 robustness of its encoding scheme (i.e. redundancy of encoding). Consistently, it is likely that
556 VP neurons display such robust encoding of valence, in large part, due to the loss of odor
557 identity information. By comparison, OT populations may be able to encode information about
558 the large olfactory identity space due to their high dimensionality. We speculate that the
559 extensive inhibitory collaterals among SPN's play a role in enforcing the high dimensionality of
560 OT activity. Though it is entirely unknown what anatomical or physiological strategies are used
561 to reduce VP dimensionality, we consider this an important piece of the puzzle in understanding
562 VP computations.
563 We saw little evidence of negative valence neurons in any of the 3 populations that were
564 imaged. This was surprising given previous reports of negative valence neurons in the VP
565 (Stephenson-Jones et al., 2020). We consider 2 potential explanations for this discrepancy.
566 First, it is possible that our conditioning paradigm was not sufficiently aversive for the animals.
567 Although our behavioral evidence for aversive association is significant, it is less robust than

568 sucrose association raising the possibility that the learning was insufficient. This could be due to
569 the fact that we targeted the airpuff to the animal's hindquarters rather than to the face. But we
570 note that in a previous report, airpuff delivery to the snout and to hindquarters elicited similar
571 ingress response in a burrowing assay (Fink et al., 2019). Additionally, we observed clear
572 unconditioned responses to the airpuff itself. Another possibility is that, while negative valence
573 neurons do exist in the VP, as has been reported, they were outside of our field-of-view.
574 Previous work in the VP supports positive and negative valence as being encoded by *Vgat*+ and
575 *Vglut2*+ neurons, respectively (Faget et al., 2018; Stephenson-Jones et al., 2020). Most *Vglut2*+
576 neurons are found in the dorsomedial portion of the VP, whereas our lenses were specifically
577 targeted to the ventrolateral portion where we found the most OT afferents. Given this
578 distinction, our results are not inconsistent with previous reports of negative valence neurons in
579 the VP.
580 In this work, we present evidence that may appear to contradict previous anatomical and
581 physiological characterizations of the OT. We find that the anteromedial portion of the OT sends
582 high-dimensional information about odor identity primarily to the VP and not the VTA. By directly
583 comparing OT and VP population-level activity in the same paradigm, we bridge together, for
584 the first time, the fields of OT and VP. This provides valuable context which not only helps us
585 evaluate past conclusions about valence encoding in the OT but also consider the implications
586 of the stimulus-evoked activity in the OT. This comparative approach leads us to conclude that
587 the OT has relatively little valence information. However, our findings are not generally
588 inconsistent with what has been observed in previous studies. We do find reward modulation in
589 the OT_{D1} population, however, we do not find valence encoding single neurons and the
590 population vector does not generalize between two rewarded odors as it does in the VP.
591 Therefore we propose that representation in the OT reflects either an intermediate
592 representation of reward-contingency or a contrast modulation to reflect the contingency.
593
594 **Speculation**
595 It is interesting to note the discrepancy between the anatomical organization of dorsal
596 striatum (DS) vs. ventral striatum (VS): SPN's of the DS project exclusively to either the
597 substantia nigra pars reticulata (SNr) of the midbrain (Drd1+) or the exterior portion of the
598 globus pallidus (GPe) (Drd2+), but Drd1+ neurons in the VS (Acb) project to both the VTA of the
599 midbrain and the ventral pallidum (Kupchik et al., 2015). The OT appears to have further limited

600 output divergence, whereby both OTD1 and OTD2 neurons project primarily to the VP. This
601 may reflect at a gradient of anatomical connectivity where the most dorsal Drd1+ SPN's project
602 primarily to the midbrain and the most ventral Drd1+ SPN's (i.e. OTD1 neurons) project primarily
603 to the pallidum. Functionally, the lack of evidence for OTD1 to midbrain connectivity challenges
604 the dichotomy of direct vs. indirect pathways in the ventral basal ganglia. In this model, DA
605 orchestrates motor initiation by oppositely modulating Drd1+ and Drd2+ SPN's, which have
606 differential downstream targets. Given the lack of clear differences in OTD1 and OTD2
607 projections, we think this canonical model of basal ganglia connectivity inadequately explains
608 the functional consequences of DA modulation in the OT.
609 In our work, we described key differences in how reward cues are encoded in 2
610 synaptically connected nuclei. But what insights can we infer about the role of OT on shaping
611 VP activity through this comparison? The most salient observation of VP activity is the large and
612 widespread excitatory responses to sucrose-cues. Though the effect size is smaller, OT_{D1}
613 neurons also showed larger excitatory responses to sucrose-cue when compared to other
614 odors. Given that these neurons are GABAergic and their primary target are the VP neurons, it
615 is difficult to explain how these 2 responses are related. We consider 3 possible explanations for
616 this paradox. First, in addition to large excitatory responses that were specific to the sucrose-
617 cues, we also observed inhibitory responses that were specific to the sucrose-cues. It is
618 possible that the excitatory VP activity during sucrose-cue presentation is driven mainly by the
619 numerous excitatory afferents (Pir, BLA, etc.) while the inhibitory VP activity is driven mainly by
620 OT_{D1} and OT_{D2} afferents. In a second model, there could be mechanisms downstream of
621 somatic activity that could explain the discrepancy. For example, though brief optical stimulation
622 of D2 neurons in Acb leads to a decrease of VP activity, prolonged activation causes an
623 increase in VP activity via the δ-opioid receptor (Soares-Cunha et al., 2020). Our experiments
624 do not provide any information on how neuropeptide release from OT neurons is different during
625 presentation of sucrose-cue vs. control odor. Similarly, we cannot measure if and how positively
626 valent stimuli change the input-output-function of OT neurons. Previous reports have found that
627 Drd2 agonism in Acb neurons leads to a decrease in collateral inhibition through a presynaptic
628 mechanism (Dobbs et al., 2016). Given that more DA is expected to be released during
629 presentation of sucrose-cues, it is plausible that the probability of GABA release from OT
630 boutons onto VP dendrites is affected. In a third and perhaps the most parsimonious model,
631 endogenous OT activity does not contribute significantly to explaining the bulk excitatory activity

632 in VP. This goes against the prevailing working model in Acb to VP circuit which assumes that
633 Acb excitation leads to VTA disinhibition by inhibiting the VP. And while there is evidence
634 supporting from bulk stimulation of D1 or D2 neurons in the Acb (Soares-Cunha et al., 2020),
635 under endogenous conditions, both Acb neurons and VP neurons are excited in response to
636 reward-cues (Lederman et al., 2021; Ottenheimer et al., 2018). Furthermore, given that
637 GABAergic synapses from SPN's to VP neurons is likely dendritic (Bolam et al., 1986), we think
638 it is unlikely that OT to VP drives large-scale shunting of action potential in the presence of
639 excitatory drive from other areas known to respond preferentially to reward cues such as the
640 BLA (Beyeler et al., 2018) or the OFC (Wang et al., 2020). We consequently propose an
641 alternate framework in which the mechanistic role of the OT in this circuit is to provide
642 spatiotemporally precise inhibition to coordinate the integration of excitatory inputs onto VP.
643 This form of inhibition could gate which excitatory synapses go through Hebbian potentiation vs.
644 anti-Hebbian depression. Under such a framework, OT would function as a high-dimensional
645 filter for VP neurons to adaptively scale its various excitatory afferents.
646
647

648 Methods

649 Stereotaxic Surgery:

650 All procedures were approved by the UCSD Institutional Animal Care and Use
651 Committee. Animals were anesthetized with isoflurane (3% for induction, 1.5-2.0% afterward)
652 and placed in a stereotaxic frame (Kopf Model 1900). Mouse blood oxygenation, heart rate and
653 breathing were monitored throughout surgery, and body temperature was regulated using a
654 heating pad (Physio Suite, Kent Scientific). A small craniotomy above the injection site was
655 made using standard aseptic technique. Virus was injected with needles pulled from capillary
656 glass (3-000-203-G/X, Drummond Scientific) at a flow rate of 2nl/s using a micropump (Nanoject
657 III, Drummond Scientific). For OT anterograde tracing experiments, 50µl of AAV9-phSyn1-
658 FLEX-tdTomato-T2A-SypEGFP-WPRE diluted to 10^{12} vg/ml was injected into the rostral portion
659 of the medial OT (AP: 1.6mm, ML: -1.0mm, DV: -5.375mm) in *Drd1*-Cre or *Adora2a*-Cre mice.
660 For VP retrograde tracing experiments, 100 nl of Cholera Toxin Subunit B CF 488A (Biotium)

661 was injected at into the caudal portion of the ventrolateral VP (AP: 0.75mm, ML: -1.4mm, DV: -
662 5.4mm) and 100 nl of Cholera Toxin Subunit B CF 543 (Biotium) was injected into the
663 dorsomedial VP (AP: 0.75mm, ML: -1.0mm, DV: -5.35mm) in C57BL6/J mice. For VTA
664 retrograde tracing experiments, 100 nl of Cholera Toxin Subunit B CF 647 (Biotium) was
665 injected to the rostral portion of the VTA (AP: -3.1mm, ML: 0.8mm, DV: -4.5mm) in C57BL6/J
666 mice. CTB injections were done at 1 mg/ml dilution in PBS. In some cases, tracers were
667 injected bilaterally and each hemisphere was analyzed independently. Following each injection,
668 the injection needle was left at the injection site for 10 minutes then slowly withdrawn.
669 For imaging experiments, the skull was prepared with OptiBond™ XTR primer and
670 adhesive (KaVo Kerr) prior to the craniotomy. After performing a craniotomy 800 um in diameter
671 centered around the virus injection site, a 27G blunt needle was used to aspirate 1.5 mm below
672 the brain surface. For OT imaging experiments, 500 ul of AAV9-syn-FLEX-jGCaMP7s-WPRE
673 (Addgene viral prep #104491-AAV9) was diluted to 10^{12} vg/ml and injected into the left and
674 rostral portion of the medial OT in D1-Cre or A2A-Cre mice. For VP imaging experiments, 300 ul
675 of AAV9-syn-jGCaMP7s-WPRE (Addgene viral prep #104487-AAV9) was diluted to 10^{12} vg/ml
676 and injected into the left and caudal portion of the ventrolateral VP in C57BL6/J mice. Following
677 the viral injection, a head-plate (Model 4, Neurotar) was secured to the mouse's skull using
678 light-curing glue (Tetric Evoflow, Ivoclar Group). At least 30 minutes after viral injection, a
679 600um GRIN lens (NA, ~1.9 pitch, GrinTech) was sterilized with Peridox-RTU then slowly
680 lowered at a rate of 500 um/min into the craniotomy until it was 200 um dorsal to the injection
681 coordinate. The lens was adhered to the surface of the skull using Tetric Evoflow. We then
682 placed a hollow threaded post (AE825ES, Thorlabs) to act as a housing for the lens and
683 adhered it using Tetric Evoflow. Any part of the skull that was still visible was covered using
684 dental cement (Lang Dental). Finally, the housing was covered with a Nylon cap nut
685 (94922A325, McMaster-Carr) screwed onto the thread post to protect the lens in between
686 imaging. Animals were left on the heating pad until they fully recovered from anesthesia.

687 Histology:

688 Mice were administered ketamine (100 mg/kg) and xylazine (10 mg/kg) and euthanized
689 by transcardial perfusion with 10 ml of cold PBS followed by 10 ml of cold 4% paraformaldehyde
690 in PBS. Brains were extracted and left in a 4% PFA solution in PBS overnight. 50 um coronal
691 sections were cut on a vibratome (VT1000, Leica). A subset of tissue was labeled using the

692 following simplified staining protocol. First, brain sections were incubated for 48 hours at 4°C in
693 the primary antibody diluted in PBST (0.3% Triton-X in PBS). Brain sections were then washed
694 3 times for 15 minutes in PBST before and after incubating for 2 hours at room temperature in
695 the secondary antibody diluted in PBST. The antibodies used in this study and their dilutions
696 are: Rb α-substance P (1:1,000 dilution; 20064, Immunostar), Rb α-TH (1:1,000 dilution;
697 AB152, Millipore), Dk α-Rb Alexa Fluor™ 488 (1:2,000 dilution; A-210206, Thermo Fisher
698 Scientific), Dk α-Rb Alexa Fluor™ 647 (1:2,000 dilution; A-31573, Thermo Fisher Scientific).
699 Slices were mounted using Fluoromount with a DAPI counterstain (SouthernBiotech) and
700 imaged on an Olympus BX61 VS120 Virtual Slide Scanner and 10x objective (Olympus). Brains
701 were harvested 21-30 days or 5-7 days after surgery for anterograde and retrograde tracing
702 experiments, respectively. Brains injected for Ca^{2+} imaging were harvested within a week of the
703 last imaging session.
704 For anterograde tracing quantification, 4-6 slices containing each of the brain regions of
705 interest (VP, LH, and VTA) were analyzed per animal. To quantify the relative abundance of OT
706 axons in a given brain region, boundaries for the region were drawn on ImageJ Fiji (National
707 Institutes of Health) with reference to the Paxinos and Franklin Mouse Brain Atlas. Afterwards,
708 the percentage of the 16-bit pixels within the boundary that had intensity above 200 was
709 quantified. For retrograde tracing experiments, cells were counted manually every 4th slice.

710 Behavior

711 Mice were water restricted to reach 85-90% of their initial body weight and given access
712 to water for 5 minutes a day in order to maintain desired weight. Prior to imaging, mice were
713 habituated to the head fixation device (Neurotar) and treadmill for 3-5 days, 15-30 minutes per
714 session. The treadmill parts were 3D printed using a LCD printer (X1-N, EPAX) from publicly
715 available designs (Jackson et al., 2018). During habituation, mice were provided 10% sucrose
716 from the water spout. Walking and licking behaviors were measured using a quadrature encoder
717 (HEDR-5420-es214, Broadcom) and a capacitance sensor (1129_1, Phidgets), respectively. A
718 video feed of the animal's face was also recorded using a camera (acA1300-30um, Basler) with
719 a 8-50mm zoom lens (C2308ZM50, Arducam) at 20 Hz with infrared illumination (VQ2121,
720 Lorex Technology).
721 Odor was delivered to the mouse using a custom-built olfactometer. Compressed
722 medical air was split into 2 gas-mass flow controllers (GFC17, Aalborg). One flow controller

723 directed a constant rate of 1.5 L/min to a hollowed out teflon cylinder. The other flow regulator
724 was connected to a 3-way solenoid valve (**LHDB1223418H,** The Lee Co.). Prior to odor delivery,
725 the 3-way valve directs clean air at 0.5 L/min to the teflon cylinder. During odor delivery, the 3-
726 way valve directs air to an odor manifold, which consists of an array of 2-way solenoid valves
727 (LHDB1242115H, The Lee Co.), each connected to a different odor bottle. Depending on the
728 trial type, the appropriate 2-way valve opens, directing 0.5 L/min of air flow through the odor
729 bottle containing a kimwipe blotted with 50 ul of diluted odor. All odors were diluted in mineral oil
730 (M5310, Sigma-Aldrich) to 1.5 mmHg. The kinetics and consistency of odor delivery were
731 characterized for 30 trials of terpinene delivery using a miniature Photoionization Detector
732 (mPID) (Aurora Scientific, Inc).
733 During classical conditioning, animals were exposed to the following odors for 2
734 seconds: 3-hexanone, 3-heptanone, 3-octanone, α-terpinene, α-pinene, and (R)-(+)-limonene
735 (all odors were purchased from Sigma with the highest available purity). In days 1-3 of training,
736 each of the 6 odors and associated outcomes were provided 30 times with 12-18 seconds of
737 inter-trial interval. Hexanone and terpinene were not associated with any outcome, heptanone
738 and pinene were associated with 2 ul of 10% sucrose, and octanone and limonene were
739 associated with a 70 psi airpuff delivered to their hindquarters. Sucrose or airpuff was delivered
740 100-300 ms after the end of odor delivery. Trials were organized into 30 blocks, each of which
741 consisted of 1 trial of each of the 6 odors in randomized order. In days 4-6 of training, the
742 outcome contingencies were switched such that heptanone and limonene were not associated
743 with any outcome, octanone and terpinene were associated with 2 ul of 10% sucrose, and
744 hexanone and pinene were associated with 70 psi airpuff.
745 In the lick-no-lick paradigm, trials were also structured into 30 blocks, each of which
746 consisted of 1 trial of each of the 6 odors in randomized order. Hexanone and terpinene were
747 not associated with any outcome, heptanone and pinene were paired with 2 ul of 10% sucrose
748 at 50% chance, and octanone and limonene were paired with 2 ul of 10% sucrose at 100%
749 chance. 200 ms prior to the onset of 3 of the odors (terpinene, octanone, and limonene), the lick
750 spout was retracted 30 mm away from the animal's mouth using a linear stepper motor (BE073-
751 1, Befenybay) and driver (A4988, BIQU). The lick spout would return to its original position 100
752 ms prior to the earliest possible time of sucrose delivery.

DeepLabCut

DeepLabCut2.3.3 with Tensorflow 2.12 was used to track 4 points on the periphery of the eye during 2-photon Ca^{2+} imaging. The mini-batch k-means clustering method was used to extract a total of 100 frames (20 frames from 5 animals). These frames were labeled and used to train a Deep Neural Network (DNN) model for 100,000 iterations. After the first training session, 20 outlier frames were picked up from each video and added to the training data for a second training session. The area of the eye at a given time point was estimated as an ellipse. For the lick-no-lick paradigm, we used DeepLabCut to track the tip of the tongue, the corner of the mouth, the upper lip and the lower lip. To record licking in the absence of the lick spout, we trained a linear classifier using logistic regression of the following metrics: 1) the confidence score for the tip of the tongue, 2) the confidence score for the corner of the mouth and 3) the Euclidean distance between the upper and lower lip. Data collected from the capacitive lick sensor was used as ground truth for the classifier.

2-photon Ca^{2+} imaging in head-fixed, behaving mice

Mice were habituated to the head-fixation setup for 3 days beginning 8-10 weeks after surgery. Ca^{2+} imaging data was acquired using an Olympus FV-MPE-RS Multiphoton microscope with Spectra Physics MaiTai HPDS laser, tuned to 920 nm with 100 fs pulse width at 80 MHz. Each 128x128 pixel scan was acquired with a 20x air objective (LCPLN20XIR, Olympus), using a Galvo-Galvo scanner at 5Hz. Stimulus delivery and behavioral measurements were controlled through a custom software written in LabVIEW (National Instruments) and operated through a DAQ (USB-6008, National Instruments). Each imaging session lasted between 30-45 minutes and was synchronized with the stimulus delivery software through a TTL pulse. The imaging depth was manually adjusted to closely match that of the first imaging day such that we recorded from overlapping populations across days of imaging. Animals were excluded from analysis if a) histology showed that either the GRIN lens or the jGCaMP7s virus was mistargeted or b) the motion during imaging was too severe for successful motion-correction. 2 animals were excluded due to mistargeting and 2 animals were excluded due to excessive motion.

Image Processing:

Ca^{2+} imaging data were first motion-corrected using the non-rigid motion correction algorithm NoRMCorre (Pnevmatikakis and Giovannucci, 2017). Afterwards, neural traces were extracted from the motion-corrected data using constrained nonnegative matrix factorization (CNMF) (Giovannucci et al., 2019; Pnevmatikakis et al., 2016). Briefly, this algorithm estimates a spatial matrix (analogous to the idea of ROI's in manual processing methods) and a temporal matrix whose products equal the motion-corrected spatiotemporal fluorescence data. Spatial components identified by CNMF were inspected by eye to ensure they were not artifacts. A Gaussian Mixture Model (GMM) was used to estimate the baseline fluorescence of each neuron. To account for potential low-frequency drift in the baseline, the GMM was applied along a moving window of 2,500 frames (500 seconds). The fluorescence of each neuron at each time point *t* was then normalized to the moving baseline to calculate $\Delta F/F = F_t - F_{baseline}/F_{baseline}$. For analysis comparing the activity of the same neuron across multiple, spatial components from two different imaging days were matched manually. All subsequent analyses were performed using custom code written in MATLAB (R2022b).

Hierarchical clustering of pooled averaged responses

ΔF/F in response to all 6 odors on day 6 were averaged across trials then Z-scored. The resulting trial-average values from the following timebins were averaged across time: 1) the first second during each odor, 2) the last second during each odor, and 3) the first second after each odor. The resulting 18-element vectors were sorted into 6 clusters after agglomerative hierarchical clustering using euclidean distance and ward linkage.

Responsiveness criteria

To determine how many neurons were responsive to a given odor, we compared ΔF/F at each frame during the 2 second odor period against a pooled distribution of ΔF/F values from the 2-seconds prior to odor onset using a Wilcoxon rank sum test. The resulting p-values were evaluated with Holm-Bonferroni correction to ensure that familywise error rate (FWER) was below 0.05. We then calculated the percentage of responsive neurons for each animal to show the mean and the standard error as a function of time. We also counted the number of neurons

809 that were significantly responsive for at least 4 frames during the odor period to report the total
810 percentage of responsive neurons during odor.

811 Single neuron logistic classifiers

812 To test how reliably a single neuron's fluorescence could discriminate between 2 odors,
813 we assessed the performance of binary logistic classifiers trained on a single neuron's
814 responses to 2 odors. For each neuron and odor pair, we averaged the ΔF/F during the last
815 second of the odor exposure for each trial then Z-scored across all trials. The resulting 60-
816 element vector was used to train a linear classifier using logistic regression. The receiver
817 operator characteristic (ROC) was evaluated for each single neuron pairwise classifier and the
818 area under the curve (AUC) reported. To test if a given pairwise classifier performed
819 significantly better than chance, we compared the accuracy of each classifier against a
820 distribution of 10,000 classifiers trained on shuffled labels.

821 Normalized ΔΔF/F correlations

822 To compare the average response of a neuron to each odor, the trial-averaged ΔF/F
823 during the last second of odor exposure from each trial was averaged and then subtracted from
824 the trial-averaged ΔF/F during the 2 seconds prior to odor delivery. This ΔΔF/F value was
825 scaled to the largest positive ΔΔF/F value of each neuron for all odors. To assess the similarity
826 of the average response to a given pair of odors i and j, we looked at the null linear model in
827 which all neurons respond identically to both odors, i.e. $\Delta\Delta F_j/F = \Delta\Delta F_i/F$. To assess how well
828 this describes the data, we report the R^2 value of the fit.

829 Pairwise euclidean distance

830 To quantify the differences among population-level responses to the 6 odors, we
831 quantified the pairwise Euclidean distance between the trajectories of odor responses. First, we
832 subtracted the ΔF/F values during the 2 seconds prior to odor delivery from each frame then
833 averaged these values across trials for each odor. The pairwise Euclidean distance at each
834 frame was computed for each odor pair and normalized to the maximum pairwise distance
835 measured in all odor pairs at any time bin. These calculations were carried out separately for

836 each animal and then averaged across biological replicates to report the mean and the standard
837 error.

838 Population pairwise classifiers

839 To assess the discriminability of odor responses in high-dimensional space, we
840 measured the accuracy of binary classifiers for a given odor pair. At each time point relative to
841 odor delivery, we pooled ΔF/F values from all trials during which either odor was presented.
842 These values were then normalized and used to train a linear classifier using either a logistic
843 regression or a Support Vector Machine (SVM). The accuracy of the classifier was evaluated via
844 5-fold cross-validation. To test if a given pairwise decoder performed significantly better than
845 chance, we compared the accuracy of each classifier against a distribution of 10,000 classifiers
846 trained on shuffled labels. All classifiers were trained on populations of neurons simultaneously
847 recorded from individual mice. The resulting cross-validated accuracies were averaged across
848 biological replicates to report the mean and the standard error.

849 Dimensionality analysis

850 To quantify the dimensionality of each simultaneously recorded neural population, we
851 calculated its participation ratio (PR). First, we performed principal component analysis of the
852 whole dataset using the singular value decomposition algorithm. The PR was calculated as the
853 square of the sum of the eigenvalues of the covariance matrix divided by the sum of the square
854 of its eigenvalues (Litwin-Kumar et al., 2017; Recanatesi et al., 2019). To account for the
855 differences in number of recorded neurons across individuals, we bootstrapped the PR by
856 randomly sampling *n* neurons from each dataset 1,000 times and reported the average PR
857 value.

858 Statistical analysis

859 For simple pairwise comparisons, we used Student's t-tests or, when appropriate,
860 Wilcoxon rank sum tests with Benjamini Hochberg correction to adjust for false discovery rate
861 (FDR). For post hoc comparisons following ANOVA's, we used Tukey's honestly significant
862 difference test which adjusts for family-wise error rate (FWER). For linear mixed-effects models

with individual animals as random effect, we used the MATLAB fitlme function with maximum likelihood estimation algorithm and Quasi-Newton optimization.

Author contributions

D.L. and C.M.R. conceived of the project, participated in its development, and wrote the manuscript. L.L. assisted with anatomy, histology and behavioral analysis. D.L. performed all imaging experiments and analyzed the data.

Acknowledgments

We thank members of Root lab for discussions, M. Aoi for discussions on data analysis, and T. Komiyama and for comments on the manuscript. This research was supported by grants from the NIH (R00DC014516, R01DC018313), and C.M.R. was a Hellman Fellow.

References

Allen WE, Chen MZ, Pichamoorthy N, Tien RH, Pachitariu M, Luo L, Deisseroth K. 2019. Thirst regulates motivated behavior through modulation of brainwide neural population dynamics. *Science* **364**:253.

Beier KT, Steinberg EE, DeLoach KE, Xie S, Miyamichi K, Schwarz L, Gao XJ, Kremer EJ, Malenka RC, Luo L. 2015. Circuit Architecture of VTA Dopamine Neurons Revealed by Systematic Input-Output Mapping. *Cell* **162**:622–634.

Beyeler A, Chang C-J, Silvestre M, Lévêque C, Namburi P, Wildes CP, Tye KM. 2018. Organization of Valence-Encoding and Projection-Defined Neurons in the Basolateral Amygdala. *Cell Rep* **22**:905–918.

Bolam JP, Ingham CA, Izzo PN, Levey AI, Rye DB, Smith AD, Wainer BH. 1986. Substance P-containing terminals in synaptic contact with cholinergic neurons in the neostriatum and basal forebrain: a double immunocytochemical study in the rat. *Brain Res* **397**:279–289.

Chu MW, Li WL, Komiyama T. 2016. Balancing the Robustness and Efficiency of Odor Representations during Learning. *Neuron* **92**:174–186.

Dan Y, Poo M-M. 2004. Spike timing-dependent plasticity of neural circuits. *Neuron* **44**:23–30.

Dobbs LK, Kaplan AR, Lemos JC, Matsui A, Rubinstein M, Alvarez VA. 2016. Dopamine Regulation of Lateral Inhibition between Striatal Neurons Gates the Stimulant Actions of Cocaine. *Neuron* **90**:1100–1113.

Faget L, Osakada F, Duan J, Ressler R, Johnson AB, Proudfoot JA, Yoo JH, Callaway EM, Hnasko TS. 2016. Afferent Inputs to Neurotransmitter-Defined Cell Types in the Ventral Tegmental Area. *Cell Rep* **15**:2796–2808.

Faget L, Zell V, Souter E, McPherson A, Ressler R, Gutierrez-Reed N, Yoo JH, Dulcis D, Hnasko TS. 2018. Opponent control of behavioral reinforcement by inhibitory and excitatory projections from the ventral pallidum. *Nat Commun* **9**:849.

Fink AJP, Axel R, Schoonover CE. 2019. A virtual burrow assay for head–fixed mice measures habituation, discrimination, exploration and avoidance without training. *Elife* **8**:e45658.

Fujimoto A, Hori Y, Nagai Y, Kikuchi E, Oyama K, Suhara T, Minamimoto T. 2019. Signaling

Incentive and Drive in the Primate Ventral Pallidum for Motivational Control of Goal-Directed Action. *J Neurosci* **39**:1793–1804.

Gadziola MA, Stetzik LA, Wright KN, Milton AJ, Arakawa K, Del Mar Cortijo M, Wesson DW. 2020. A Neural System that Represents the Association of Odors with Rewarded Outcomes and Promotes Behavioral Engagement. *Cell Rep* **32**:107919.

Gadziola MA, Tylicki KA, Christian DL, Wesson DW. 2015. The olfactory tubercle encodes odor valence in behaving mice. *J Neurosci* **35**:4515–4527.

Giovannucci A, Friedrich J, Gunn P, Kalfon J, Brown BL, Koay SA, Taxidis J, Najafi F, Gauthier JL, Zhou P, Khakh BS, Tank DW, Chklovskii DB, Pnevmatikakis EA. 2019. CaImAn an open source tool for scalable calcium imaging data analysis. *Elife* **8**. doi:10.7554/eLife.38173

Groenewegen HJ, Russchen FT. 1984. Organization of the efferent projections of the nucleus accumbens to pallidal, hypothalamic, and mesencephalic structures: a tracing and immunohistochemical study in the cat. *J Comp Neurol* **223**:347–367.

Gubner NR, Wilhelm CJ, Phillips TJ, Mitchell SH. 2010. Strain differences in behavioral inhibition in a Go/No-go task demonstrated using 15 inbred mouse strains. *Alcohol Clin Exp Res* **34**:1353–1362.

Haberly LB, Price JL. 1977. The axonal projection patterns of the mitral and tufted cells of the olfactory bulb in the rat. *Brain Res* **129**:152–157.

Hollerman JR, Schultz W. 1998. Dopamine neurons report an error in the temporal prediction of reward during learning. *Nat Neurosci* **1**:304–309.

Igarashi KM, Ieki N, An M, Yamaguchi Y, Nagayama S, Kobayakawa K, Kobayakawa R, Tanifuji M, Sakano H, Chen WR, Mori K. 2012. Parallel mitral and tufted cell pathways route distinct odor information to different targets in the olfactory cortex. *J Neurosci* **32**:7970–7985.

Ikemoto S. 2007. Dopamine reward circuitry: two projection systems from the ventral midbrain to the nucleus accumbens-olfactory tubercle complex. *Brain Res Rev* **56**:27–78.

Ikemoto S. 2003. Involvement of the olfactory tubercle in cocaine reward: intracranial self-administration studies. *J Neurosci* **23**:9305–9311.

In ’t Zandt EE, Cansler HL, Denson HB, Wesson DW. 2019. Centrifugal Innervation of the Olfactory Bulb: A Reappraisal. *eNeuro* **6**. doi:10.1523/ENEURO.0390-18.2019

Jackson J, Karnani MM, Zemelman BV, Burdakov D, Lee AK. 2018. Inhibitory Control of Prefrontal Cortex by the Claustrum. *Neuron* **99**:1029–1039.e4.

Jones DL, Mogenson GJ. 1980. Nucleus accumbens to globus pallidus GABA projection: electrophysiological and iontophoretic investigations. *Brain Res* **188**:93–105.

Kupchik YM, Brown RM, Heinsbroek JA, Lobo MK, Schwartz DJ, Kalivas PW. 2015. Coding the direct/indirect pathways by D1 and D2 receptors is not valid for accumbens projections. *Nat Neurosci* **18**:1230–1232.

Lederman J, Lardeux S, Nicola SM. 2021. Vigor Encoding in the Ventral Pallidum. *eNeuro* **8**. doi:10.1523/ENEURO.0064-21.2021

Litwin-Kumar A, Harris KD, Axel R, Sompolinsky H, Abbott LF. 2017. Optimal Degrees of Synaptic Connectivity. *Neuron* **93**:1153–1164.e7.

Martiros N, Kapoor V, Kim SE, Murthy VN. 2022. Distinct representation of cue-outcome association by D1 and D2 neurons in the ventral striatum’s olfactory tubercle. *Elife* **11**. doi:10.7554/eLife.75463

Mathis A, Mamidanna P, Cury KM, Abe T, Murthy VN, Mathis MW, Bethge M. 2018. DeepLabCut: markerless pose estimation of user-defined body parts with deep learning. *Nat Neurosci* **21**:1281–1289.

Millman DJ, Murthy VN. 2020. Rapid Learning of Odor–Value Association in the Olfactory

Striatum. *J Neurosci* **40**:4335–4347.
Murata K, Kinoshita T, Fukazawa Y, Kobayashi K, Yamanaka A, Hikida T, Manabe H, Yamaguchi M. 2019. Opposing Roles of Dopamine Receptor D1- and D2-Expressing Neurons in the Anteromedial Olfactory Tubercle in Acquisition of Place Preference in Mice. *Front Behav Neurosci* **13**:50.
Newman R, Winans SS. 1980. An experimental study of the ventral striatum of the golden hamster. II. Neuronal connections of the olfactory tubercle. *J Comp Neurol* **191**:193–212.
Oettl L-L, Scheller M, Filosa C, Wieland S, Haag F, Loeb C, Durstewitz D, Shusterman R, Russo E, Kelsch W. 2020. Phasic dopamine reinforces distinct striatal stimulus encoding in the olfactory tubercle driving dopaminergic reward prediction. *Nat Commun* **11**:3460.
Ottenheimer DJ, Bari BA, Sutlief E, Fraser KM, Kim TH, Richard JM, Cohen JY, Janak PH. 2020a. A quantitative reward prediction error signal in the ventral pallidum. *Nat Neurosci* **23**:1267–1276.
Ottenheimer DJ, Wang K, Tong X, Fraser KM, Richard JM, Janak PH. 2020b. Reward activity in ventral pallidum tracks satiety-sensitive preference and drives choice behavior. *Sci Adv* **6**. doi:10.1126/sciadv.abc9321
Ottenheimer D, Richard JM, Janak PH. 2018. Ventral pallidum encodes relative reward value earlier and more robustly than nucleus accumbens. *Nat Commun* **9**:4350.
Pnevmatikakis EA, Giovannucci A. 2017. NoRMCorre: An online algorithm for piecewise rigid motion correction of calcium imaging data. *J Neurosci Methods* **291**:83–94.
Pnevmatikakis EA, Soudry D, Gao Y, Machado TA, Merel J, Pfau D, Reardon T, Mu Y, Lacefield C, Yang W, Ahrens M, Bruno R, Jessell TM, Peterka DS, Yuste R, Paninski L. 2016. Simultaneous Denoising, Deconvolution, and Demixing of Calcium Imaging Data. *Neuron* **89**:285–299.
Recanatesi S, Ocker GK, Buice MA, Shea-Brown E. 2019. Dimensionality in recurrent spiking networks: Global trends in activity and local origins in connectivity. *PLoS Comput Biol* **15**:e1006446.
Rescorla RA. 1972. A theory of Pavlovian conditioning : Variations in the effectiveness of reinforcement and non-reinforcement. *Classical conditioning, Current research and theory* **2**:64–69.
Ricardo JA. 1980. Efferent connections of the subthalamic region in the rat. I. The subthalamic nucleus of Luys. *Brain Res* **202**:257–271.
Richard JM, Ambroggi F, Janak PH, Fields HL. 2016. Ventral Pallidum Neurons Encode Incentive Value and Promote Cue-Elicited Instrumental Actions. *Neuron* **90**:1165–1173.
Schultz W, Dayan P, Montague PR. 1997. A neural substrate of prediction and reward. *Science* **275**:1593–1599.
Scott JW. 1981. Electrophysiological identification of mitral and tufted cells and distributions of their axons in olfactory system of the rat. *J Neurophysiol* **46**:918–931.
Shannon CE. 1948. A mathematical theory of communication. *The Bell System Technical Journal* **27**:379–423.
Smith KS, Tindell AJ, Aldridge JW, Berridge KC. 2009. Ventral pallidum roles in reward and motivation. *Behav Brain Res* **196**:155–167.
Soares-Cunha C, de Vasconcelos NAP, Coimbra B, Domingues AV, Silva JM, Loureiro-Campos E, Gaspar R, Sotiropoulos I, Sousa N, Rodrigues AJ. 2020. Nucleus accumbens medium spiny neurons subtypes signal both reward and aversion. *Mol Psychiatry* **25**:3241–3255.
Stephenson-Jones M, Bravo-Rivera C, Ahrens S, Furlan A, Xiao X, Fernandes-Henriques C, Li B. 2020. Opposing Contributions of GABAergic and Glutamatergic Ventral Pallidal Neurons to Motivational Behaviors. *Neuron* **105**:921–933.e5.

1003 Sutton RS. 1988. Learning to predict by the methods of temporal differences. *Mach Learn* **3**:9–
1004 44.
1005 Tachibana Y, Hikosaka O. 2012. The primate ventral pallidum encodes expected reward value
1006 and regulates motor action. *Neuron* **76**:826–837.
1007 Tindell AJ, Smith KS, Berridge KC, Aldridge JW. 2005. VP neurons integrate learning and
1008 physiological signals to code incentive salience of conditioned cues. *Soc Neurosci Abstr*.
1009 Tindell AJ, Smith KS, Peciña S, Berridge KC, Aldridge JW. 2006. Ventral pallidum firing codes
1010 hedonic reward: when a bad taste turns good. *J Neurophysiol* **96**:2399–2409.
1011 Tritsch NX, Sabatini BL. 2012. Dopaminergic modulation of synaptic transmission in cortex and
1012 striatum. *Neuron* **76**:33–50.
1013 Turner MS, Lavin A, Grace AA, Napier TC. 2001. Regulation of limbic information outflow by the
1014 subthalamic nucleus: excitatory amino acid projections to the ventral pallidum. *J Neurosci*
1015 **21**:2820–2832.
1016 Wang PY, Boboila C, Chin M, Higashi-Howard A, Shamash P, Wu Z, Stein NP, Abbott LF, Axel
1017 R. 2020. Transient and Persistent Representations of Odor Value in Prefrontal Cortex.
1018 *Neuron* **108**:209–224.e6.
1019 Watabe-Uchida M, Zhu L, Ogawa SK, Vamanrao A, Uchida N. 2012. Whole-brain mapping of
1020 direct inputs to midbrain dopamine neurons. *Neuron* **74**:858–873.
1021 Wesson DW. 2020. The Tubular Striatum. *J Neurosci* **40**:7379–7386.
1022 Wesson DW, Wilson DA. 2010. Smelling Sounds: Olfactory–Auditory Sensory Convergence in
1023 the Olfactory Tubercle. *J Neurosci* **30**:3013–3021.
1024 Wieland S, Schindler S, Huber C, Köhr G, Oswald MJ, Kelsch W. 2015. Phasic Dopamine
1025 Modifies Sensory-Driven Output of Striatal Neurons through Synaptic Plasticity. *J Neurosci*
1026 **35**:9946–9956.
1027 Zahm DS, Heimer L. 1987. The ventral striatopallidothalamic projection. III. Striatal cells of the
1028 olfactory tubercle establish direct synaptic contact with ventral pallidal cells projecting to
1029 mediodorsal thalamus. *Brain Res* **404**:327–331.
1030 Zhang Z, Liu Q, Wen P, Zhang J, Rao X, Zhou Z, Zhang H, He X, Li J, Zhou Z, Xu X, Zhang X,
1031 Luo R, Lv G, Li H, Cao P, Wang L, Xu F. 2017a. Activation of the dopaminergic pathway
1032 from VTA to the medial olfactory tubercle generates odor-preference and reward. *Elife* **6**.
1033 doi:10.7554/eLife.25423
1034 Zhang Z, Zhang H, Wen P, Zhu X, Wang L, Liu Q, Wang J, He X, Wang H, Xu F. 2017b. Whole-
1035 Brain Mapping of the Inputs and Outputs of the Medial Part of the Olfactory Tubercle. *Front*
1036 *Neural Circuits* **11**:52.
1037 Zhou L, Furuta T, Kaneko T. 2003. Chemical organization of projection neurons in the rat
1038 accumbens nucleus and olfactory tubercle. *Neuroscience* **120**:783–798.

Figure 1:

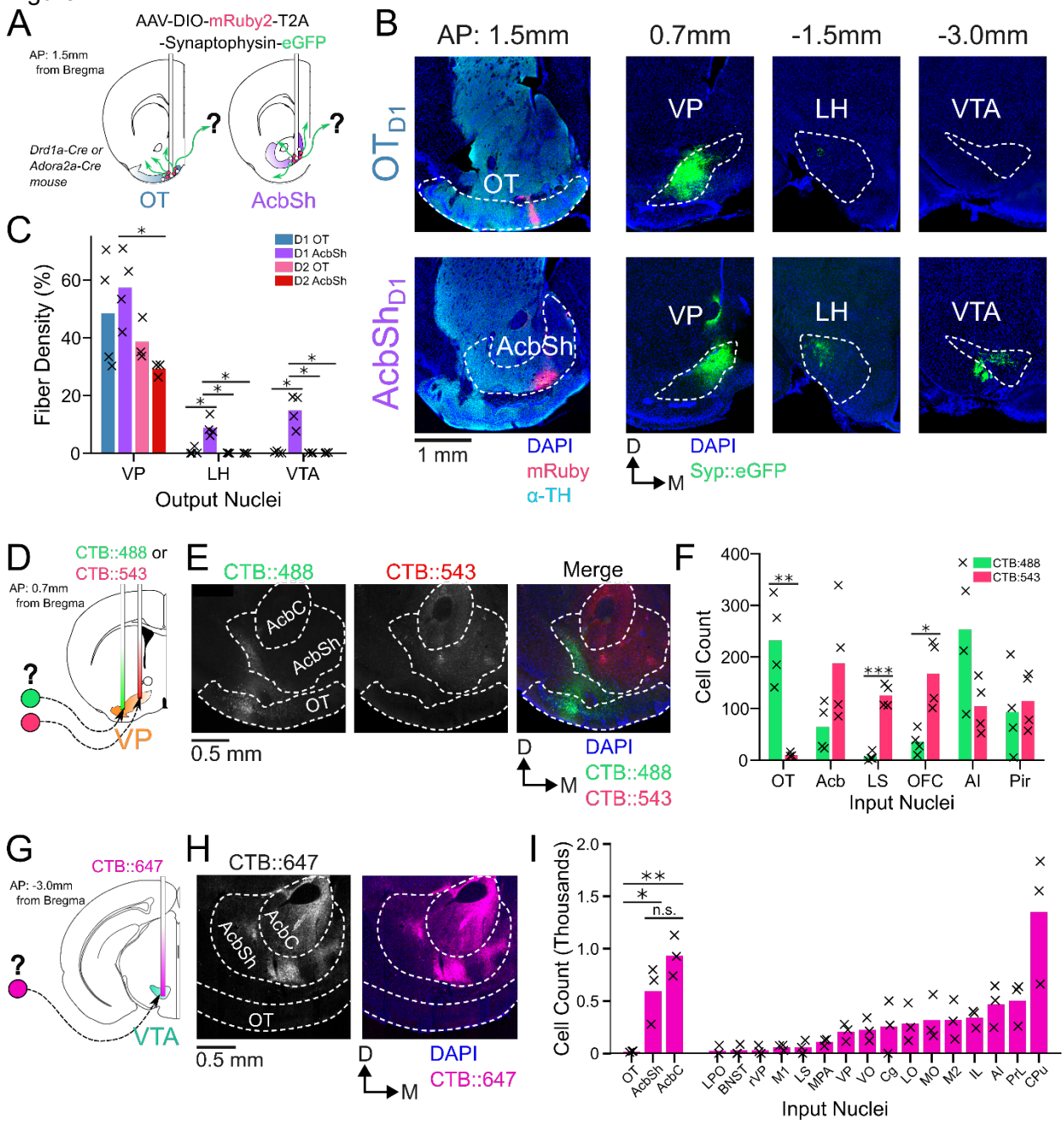
A
AAV-DIO-mRuby2-T2A
-Synaptophysin-eGFP
AP: 1.5mm
from Bregma
Drd1a-Cre or
Adora2a-Cre
mouse
OT
AcbSh
B
AP: 1.5mm
0.7mm
-1.5mm
-3.0mm
OT D1
AcbSh D1
OT
VP
LH
VTA
AcbSh
1 mm
DAPI
mRuby
α-TH
D
M
DAPI
Syp::eGFP
C
Fiber Density (%)
D1 OT
D1 AcbSh
D2 OT
D2 AcbSh
VP
LH
VTA
Output Nuclei
D
CTB::488 or
CTB::543
AP: 0.7mm
from Bregma
VP
E
CTB::488
CTB::543
Merge
AcbC
AcbSh
OT
0.5 mm
D
M
DAPI
CTB::488
CTB::543
F
Cell Count
CTB:488
CTB:543
OT
Acb
LS
OFC
AI
Pir
Input Nuclei
G
CTB::647
AP: -3.0mm
from Bregma
VTA
H
CTB::647
AcbSh
AcbC
OT
0.5 mm
D
M
DAPI
CTB::647
I
Cell Count (Thousands)
n.s.
OT
AcbSh
AcbC
LPO
BNST
rVP
M1
LS
MPA
VP
VO
Cg
LO
MO
M2
IL
AI
PrL
CPu
Input Nuclei

Figure 1. OT_{D1} and OT_{D2} primarily project to the lateral portion of the VP. (**A**) Schematic representation of Cre-dependent anterograde axonal AAV tracing experiments used to characterize outputs of OT neurons. *Drd1*+ and *Drd2*+ neurons were separately labeled by using *Drd1*-Cre and *Adora2a*-Cre mouse lines, respectively. (**B**) Representative images from OT_{D1} (top) vs. the $AcbSh_{D1}$ injection (bot). Target sites (far-left column) are stained with α-tyrosine hydroxylase antibodies to visualize the boundary between VP and OT. (**C**) Quantifying the % of output regions with fluorescence (n=3-4). (**D**) Schematic representation of 2-color retrograde CTB tracing experiment used to confirm OT to VP connectivity. CTB::488 and CTB::543 were injected to the lateral and medial portion of the VP, respectively. (**E**) Representative images of CTB labeled neurons in the OT and Acb. (**F**) The number of labeled cells was quantified (n=4). (**G**) Schematic representation of retrograde CTB tracing experiment used to test OT to VTA connectivity. CTB::647 was injected in the VTA. (**H**) Representative image shows robust AcbSh and AcbC labeling but no OT labeling. (**I**) Quantification of labeling in different nuclei (n=3). Pairwise comparisons were done using the Student's t-test. The p-values were corrected for FDR by Benjamini-Hocherg procedure. ***$p<0.001$, **$p<0.01$, *$p<0.05$. See Tables S1-S3 for detailed statistics.

Figure 2:

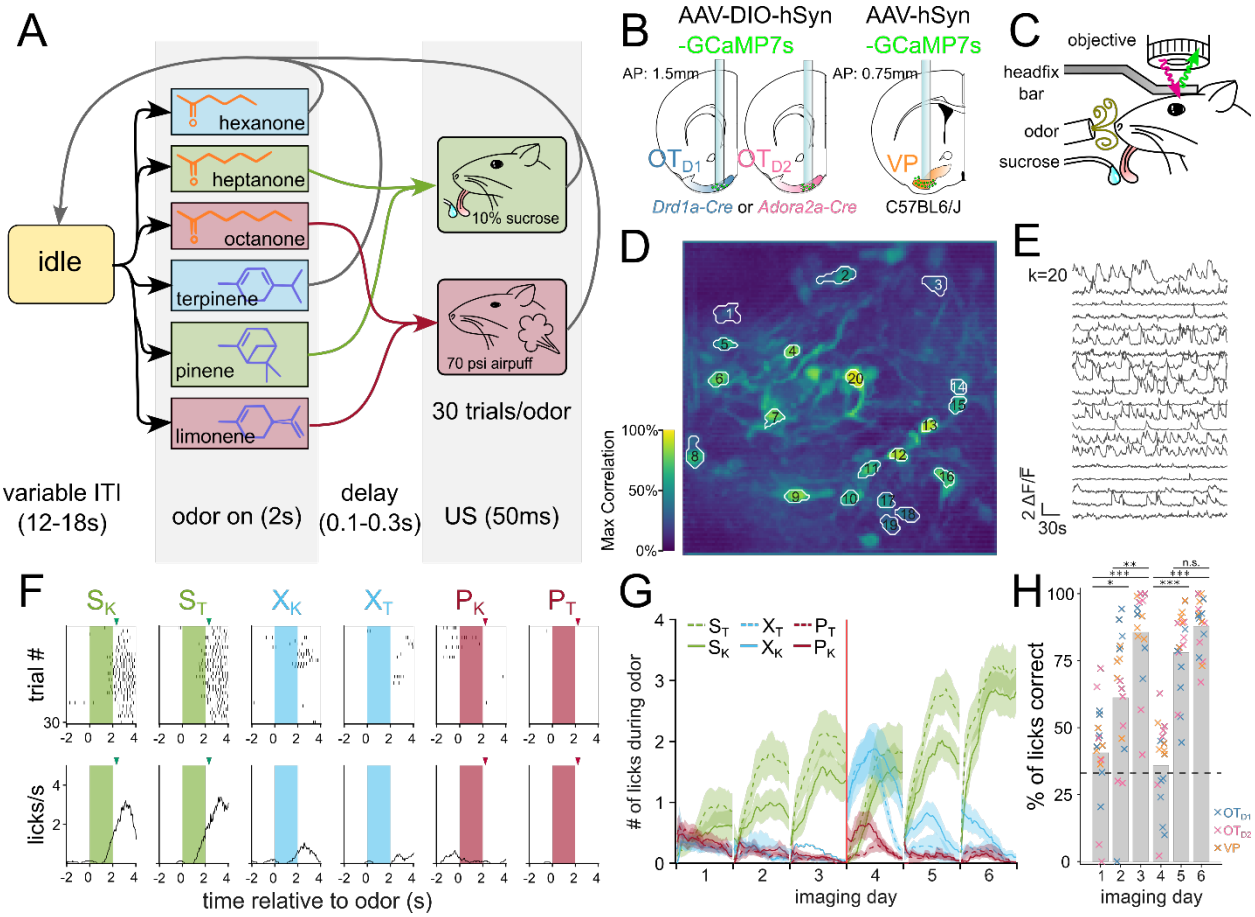
A
hexanone
heptanone
octanone
terpinene
pinene
limonene
idle
10% sucrose
70 psi airpuff
30 trials/odor
variable ITI
(12-18s)
odor on (2s)
delay
(0.1-0.3s)
US (50ms)
B
AAV-DIO-hSyn
-GCaMP7s
AAV-hSyn
-GCaMP7s
AP: 1.5mm
AP: 0.75mm
OTD1
OTD2
VP
Drd1a-Cre or Adora2a-Cre
C57BL6/J
C
objective
headfix
bar
odor
sucrose
D
Max Correlation
100%
50%
0%
E
k=20
2 ΔF/F
30s
F
SK
ST
XK
XT
PK
PT
trial #
licks/s
time relative to odor (s)
G
# of licks during odor
imaging day
H
% of licks correct
imaging day
n.s.

Figure 2. Head-fixed 2-photon Ca^{2+} imaging of OT_{D1}, OT_{D2}, or VP neurons during 6-odor conditioning paradigm. (**A**) State-diagram of odor conditioning paradigm. Each trial begins with 2 seconds of odor delivery. Odors are chosen in pseudorandomized order such that the same odor is not repeated more than twice in a row. At the end of odor delivery, there is a variable delay (100-300ms), after which the animal is given either a 10% sucrose solution (S_K and S_T), a 70 psi airpuff (P_K and P_T), or nothing (X_K and X_T). Trials are separated by a variable intertrial interval (ITI; 12-18s). Schematic representation of (**B**) lens implant surgery and (**C**) headfix 2-photon microscopy setup. An example of spatial (**D**) and temporal (**E**) components extracted by CNMF from *Drd1*-Cre animal on day 3 of imaging. (**D**) The spatial footprints of 20 example neurons are shown on top of a maximum-correlation pixel image that was used to seed the factorization. The number displayed over each neuron matches the row number of the temporal components in (**E**). (**F**) An example raster plot (top) and averaged-across-trials trace (bottom) of the licking behavior recorded concurrently as (**D**) and (**E**). The timing of odor delivery is shown as shaded rectangles. The timing of US delivery is shown as arrowheads. (**G**) The mean total licks during each of the odors is shown averaged across all animals (n=17) after application of a moving-average filter with a window size of 10 trials. Red line marks the sucrose and airpuff contingency switch between day 3 and day 4. (**H**) Bar graph showing the licks during either sucrose cue expressed as a fraction of all licks during any odor. FWER-adjusted statistical significance for post hoc comparisons are shown as: ***$p<0.001$, **$p<0.01$, *$p<0.05$. See Tables S4-5 for detailed statistics.

Figure 3:

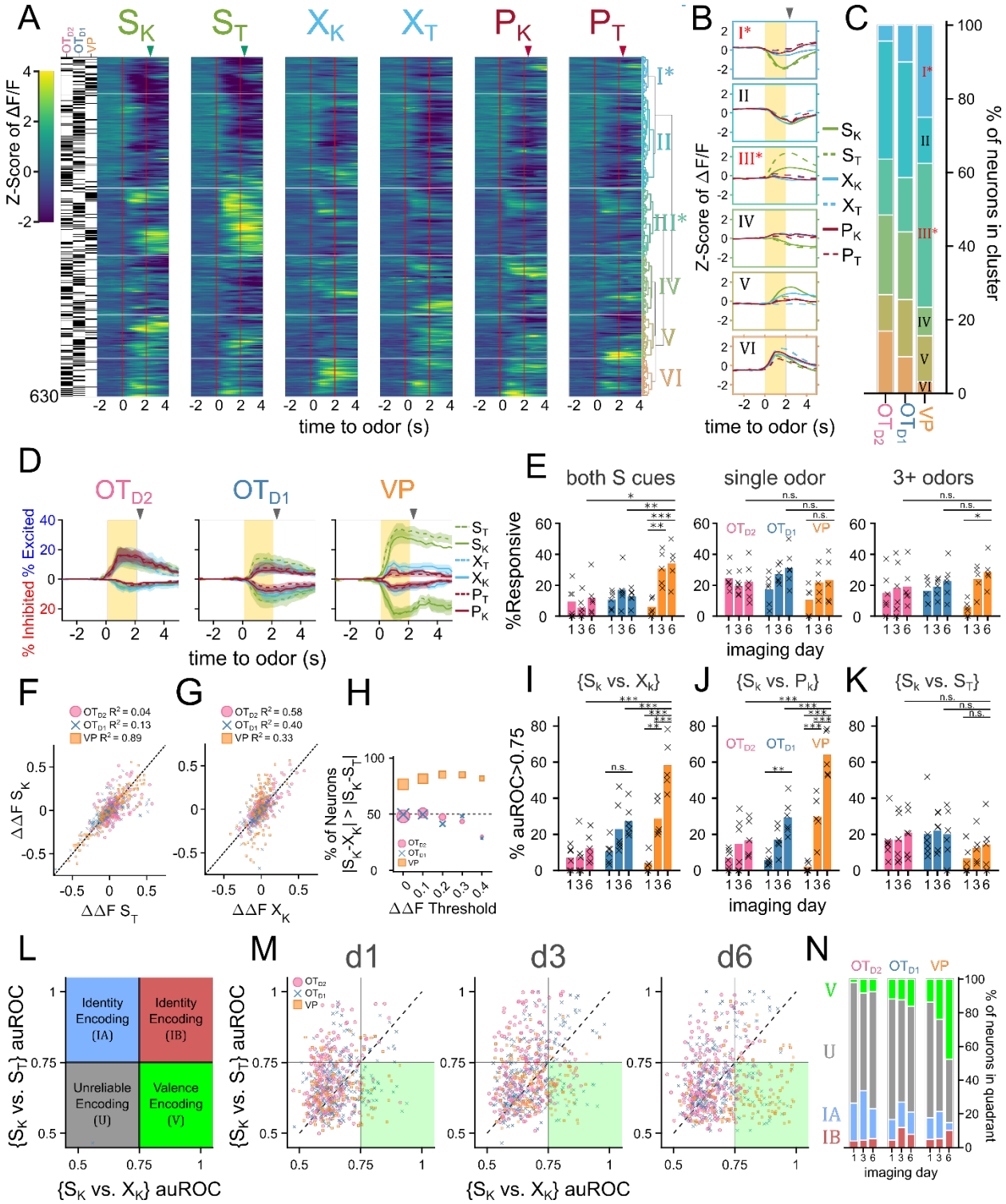
A
B
C
D
E
F
G
H
I
J
K
L
M
N
Z-Score of ΔF/F
time to odor (s)
% of neurons in cluster
% Inhibited % Excited
%Responsive
imaging day
both S cues
single odor
3+ odors
ΔΔF S_K
ΔΔF S_T
ΔΔF X_K
% of Neurons
ΔΔF Threshold
% auROC>0.75
{S_K vs. X_K}
{S_K vs. P_K}
{S_K vs. S_T}
Identity Encoding (IA)
Identity Encoding (IB)
Unreliable Encoding (U)
Valence Encoding (V)
{S_K vs. S_T} auROC
{S_K vs. X_K} auROC
d1
d3
d6
% of neurons in quadrant

Figure 3. VP neurons encode reward-contingency more robustly than OT_{D1} or OT_{D2} neurons. (**A**) Heatmap of odor-evoked activities in OT_{D1}, OT_{D2}, and VP neurons from day 6 of imaging. The fluorescence measurements from each neuron were averaged over trials, Z-scored, then pooled for hierarchical clustering. Neurons are grouped by similarity, with the dendrogram shown on the right and a raster plot on the left indicating which region a given neuron is from. Horizontal white lines demarcate the boundaries between the 6 clusters. Odor delivered at 0-2 seconds marked by vertical red lines and US delivery is marked by arrowheads. From left to right, the columns represent neural responses to sucrose-paired ketone and terpene, control ketone and terpene, and airpuff-paired ketone and terpene (S_K, S_T, X_K, X_T, P_K, P_T). (**B**) Average Z-scored activity of each cluster to each of the 6 odors on day 6 of imaging. Yellow bar indicates 2-seconds of odor exposure. (**C**) The distribution of clusters by population. (**D**) Percentage of total neurons that were significantly excited or inhibited by each odor (Bonferroni-adjusted FDR < 0.05) as a function of time relative to odor. Lines represent the mean across biological replicates and the shaded area reflects the mean ± SEM. (**E**) Bar graph showing % of neurons from each population that are responsive to both sucrose-paired odors in the same direction (left), responsive to only a single odor (middle), or responsive to at least 3 odors (right). Bars represent the mean across biological replicates and x's mark individual animals. (**F**) Scatterplot comparing the magnitudes of S_K responses ($\Delta\Delta S_K$) to S_T responses ($\Delta\Delta S_T$). The dotted line represents the hypothetical scenario where $\Delta\Delta S_K = \Delta\Delta S_T$. For each population, the R^2 value of the 2-d distribution compared to the $\Delta\Delta S_K = \Delta\Delta S_T$ line is reported. (**G**) Same as F but comparing $\Delta\Delta S_K$ to $\Delta\Delta X_K$. (**H**) Lineplot showing the % of neurons from each population where the difference between $\Delta\Delta S_K$ and $\Delta\Delta X_K$ is lower than that between $\Delta\Delta S_K$ and $\Delta\Delta S_T$. (**I**) Bargraph showing % of neurons whose responses to {S_K vs. X_K} can be discriminated by a linear classifier with auROC>0.75. (**J**) Same as (I) but for {S_K vs P_K}. (**K**) Same as (I) but for {S_K vs S_T}. (**L**) Schematic representation of 4 possible categories for a joint-distribution of {S_K vs. X_K} and {S_K vs. S_T} auROC values. Identity-encoding neurons could be in any quadrant other than the bottom-left whereas valence-encoding neurons should be in the bottom-right quadrant. (**M**) Scatterplot of each neuron's auROC value for {S_K vs. X_K} on the x-axis and {S_K vs. S_T} on the y-axis on days 1, 3 and 6 of imaging. (**N**) Stacked bar graph showing the distribution of neurons from each population that fall into each of the 4 quadrants across the 3 different imaging days. FWER-adjusted statistical significance for post hoc comparisons are shown as: ***p<0.001, **p<0.01, *p<0.05, n.s. p>0.05. See Tables S6-17 for detailed statistics.

Figure 4:

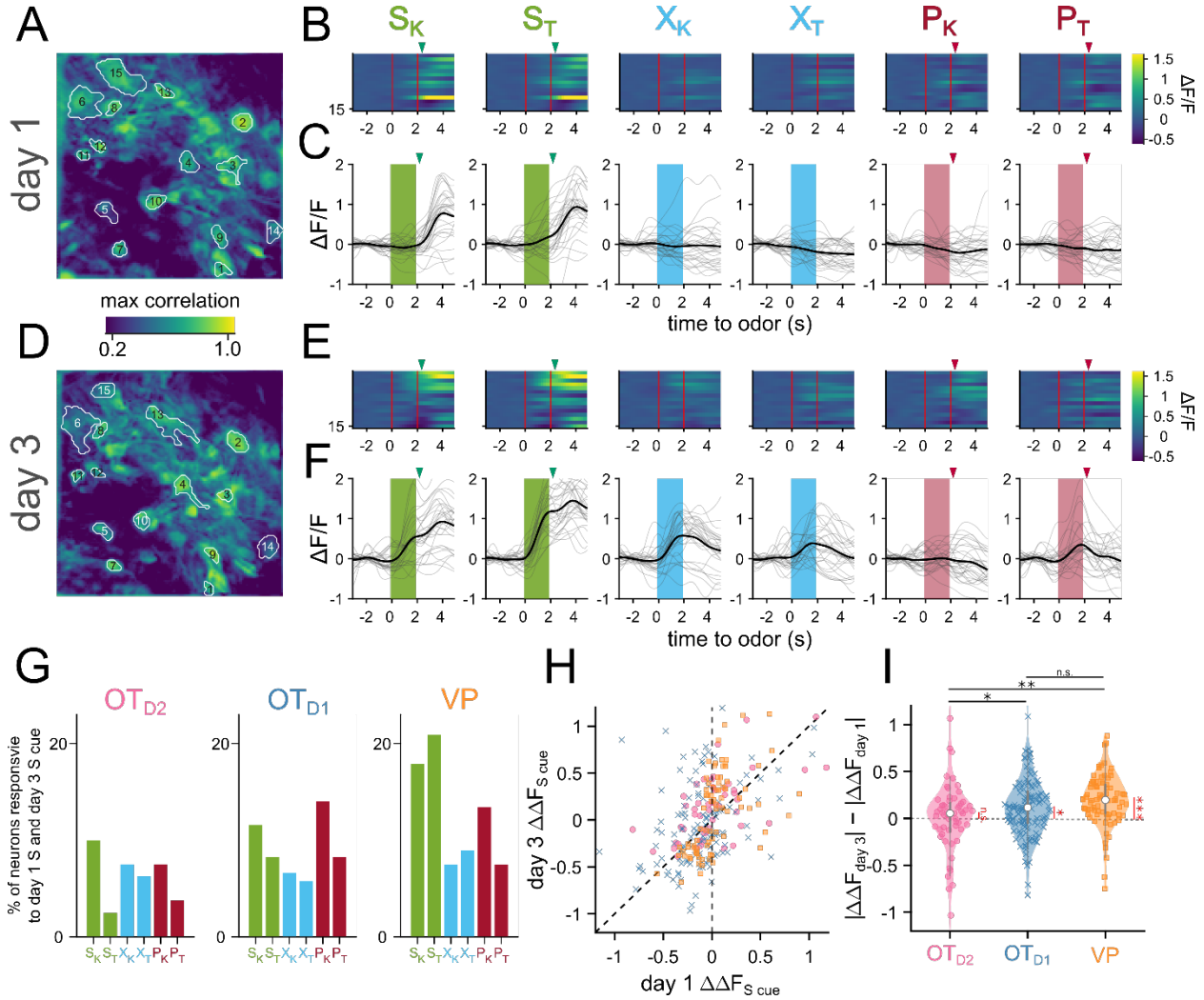
A
day 1
max correlation
0.2
1.0
B
C
D
day 3
E
F
ΔF/F
time to odor (s)
G
OT$_{D2}$
OT$_{D1}$
VP
% of neurons responsvie to day 1 S and day 3 S cue
H
day 3 ΔΔF$_{S\ cue}$
day 1 ΔΔF$_{S\ cue}$
I
|ΔΔF$_{day\ 3}$| − |ΔΔF$_{day\ 1}$|
n.s.

Figure 4. Sucrose responsive VP neurons become sucrose-cue responsive after pairing. (**A**) The spatial footprints of 15 neurons from day 1 are outlined over a max-correlation projection image. (**B**) Heatmap of averaged-over-trials ΔF/F in response to 6 odors on day 1. Odor delivery period is shown with 2 red vertical lines and sucrose/airpuff timing is shown with downward arrowhead. (**C**) An example neuron's responses on day 1 across 30 trials to 6 different odors. Individual trial traces are shown in light gray whereas the averaged-across trials trace is shown in black. Odor delivery period is depicted as shaded rectangles and US delivery is marked by arrowheads. (**D-F**) Same as (**A-C**), respectively, but for day 3. (**G**) Percentage of all tracked neurons that were both sucrose-responsive on day 1 and odor-responsive in the same direction on day 3. (**H**) Scatter plot of averaged-over-trials responses to S_K or S_T on day 1 (x-axis) and day 3 (y-axis). Each point is a neuron that was successfully matched from day 1 and day 3. Neurons from OT_{D2}, OT_{D1}, and VP are plotted as pink circles, blue crosses, and yellow squares, respectively. Neurons that have increased response magnitudes on day 3 would fall between the 2 dotted lines. (**I**) Violin plot showing the distributions of day 3 responsive magnitude – day 1 response magnitude. Black asterisks show statistical significance of pairwise comparisons and red asterisks show statistical significance for one-sample t-tests. Pairwise comparisons were done using the Student's t-test. The p-values were corrected for FDR by Benjamini-Hocherg procedure. ***$p<0.001$, **$p<0.01$, *$p<0.05$, n.s. $p>0.05$. See Tables S18-19 for detailed statistics.

Figure 5:

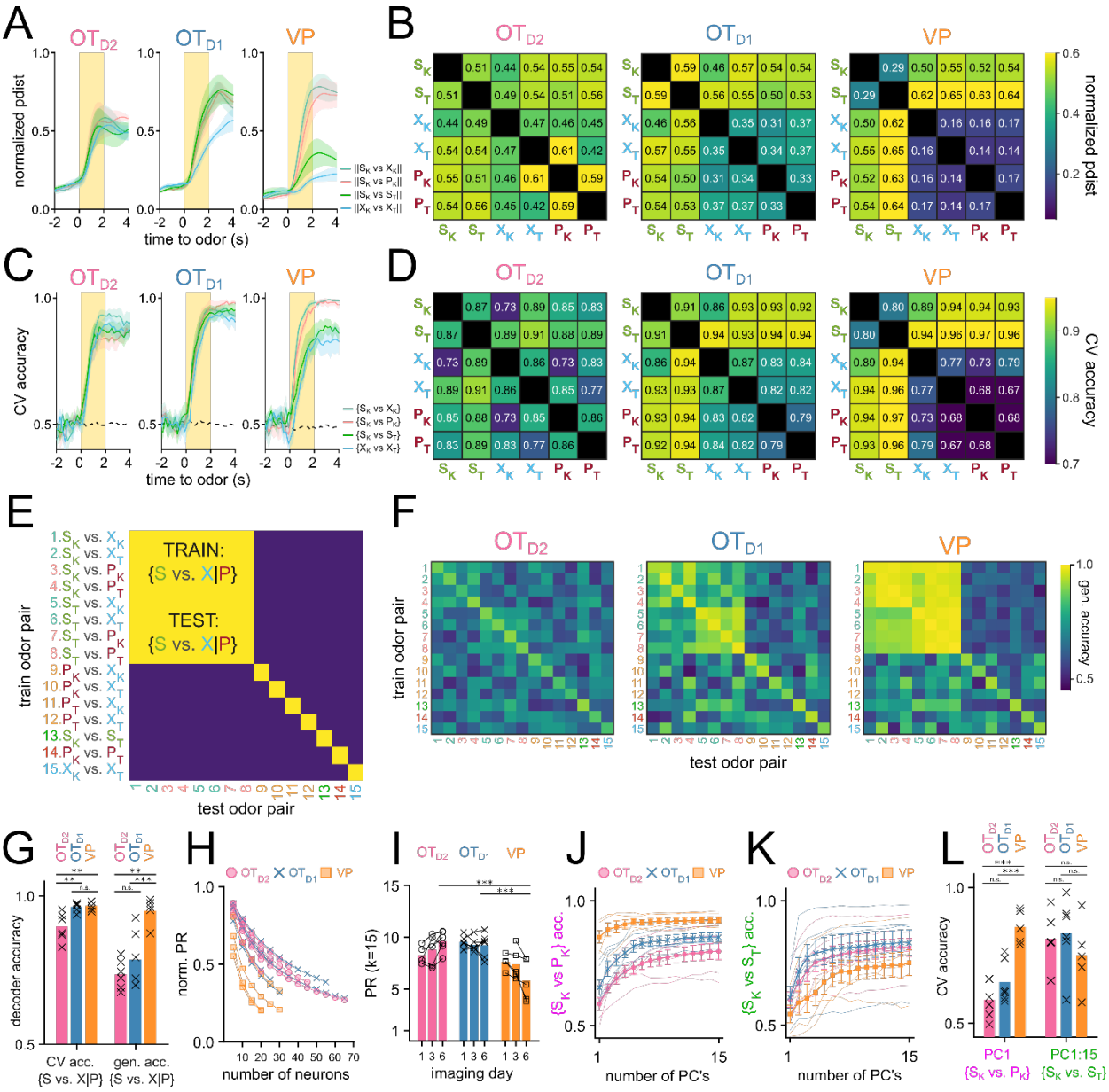
A
OTD2
OTD1
VP
normalized pdist
time to odor (s)
B
normalized pdist
C
CV accuracy
time to odor (s)
D
CV accuracy
E
TRAIN:
{S vs. X|P}
TEST:
{S vs. X|P}
train odor pair
test odor pair
F
train odor pair
test odor pair
gen. accuracy
G
decoder accuracy
CV acc. {S vs. X|P}
gen. acc. {S vs. X|P}
H
norm. PR
number of neurons
I
PR (k=15)
imaging day
J
number of PC's
K
number of PC's
L
CV accuracy
PC1 {SK vs. PK}
PC1:15 {SK vs. ST}

Figure 5. OT encodes odor identity in high-dimensional space and VP encodes reward-contingency in low-dimensional space. (**A**) Average normalized pairwise Euclidean distance between odor-evoked population-level activity from day 6 of imaging shown as a function of time relative to odor delivery. Traces show the average value across biological replicates of the same population and the shaded areas represent the average ± SEM. (**B**) A heatmap of the average normalized pairwise distance during the odor delivery period. (**C**) Average CV accuracy of binary pairwise linear classifiers trained on population data plotted against time relative to odor delivery. (**D**). A heatmap of the average CV accuracy during the odor delivery period. (**E**) Schematic representation of generalized linear classification performance for an idealized valence encoder. Each row corresponds to the training odor-pair and each column corresponds to the testing odor-pair. For an idealized valence encoder, the decodability would generalize well across odor-pairs of the equal valence grouping outlined in red. Note that the elements along the diagonal are cases where training and testing odor-pairs are identical and do not reflect generalizability. (**F**) Heatmap representing the maximum generalized linear classification accuracy during odor delivery period averaged across biological replicates for each population. (**G**) Mean cross-validated linear classifier accuracy for S-cue vs. control or puff-cue classification and the generalized accuracy for S-cue vs. control or puff-cue classification after training on a different pair. Bar represents the mean across biological replicates and x's mark accuracy values for individual animals. (**H**) Average PR normalized to *n* calculated after randomly subsampling an increasing number of neurons. (**I**) Average PR calculated after subsampling 15 neurons. (**J**) Average CV accuracy of linear classifiers trained on $\{S_K$ vs. $P_K\}$ plotted against number of principal components used for training. For each simultaneously imaged group of neurons, 15 neurons were subsampled and classifiers were trained on an increasing number of principal components. Thinner faded lines show mean accuracy across subsampling for individual animals. Markers represent the mean across biological replicates. Error bars indicate SEM across biological replicates. (**K**) Average CV accuracy of linear classifiers trained on $\{S_K$ vs. $S_T\}$. (**L**) Comparison of the average accuracy of $\{S_K$ vs. $P_K\}$ classifiers trained on the 1st PC vs. $\{S_K$ vs. $S_T\}$ classifiers trained on all 15 PC's. FWER-adjusted statistical significance for post hoc comparisons are shown as: ***$p<0.001$, **$p<0.01$, *$p<0.05$, n.s. $p>0.05$. See Tables S20-29 for detailed statistics.

Figure 6:

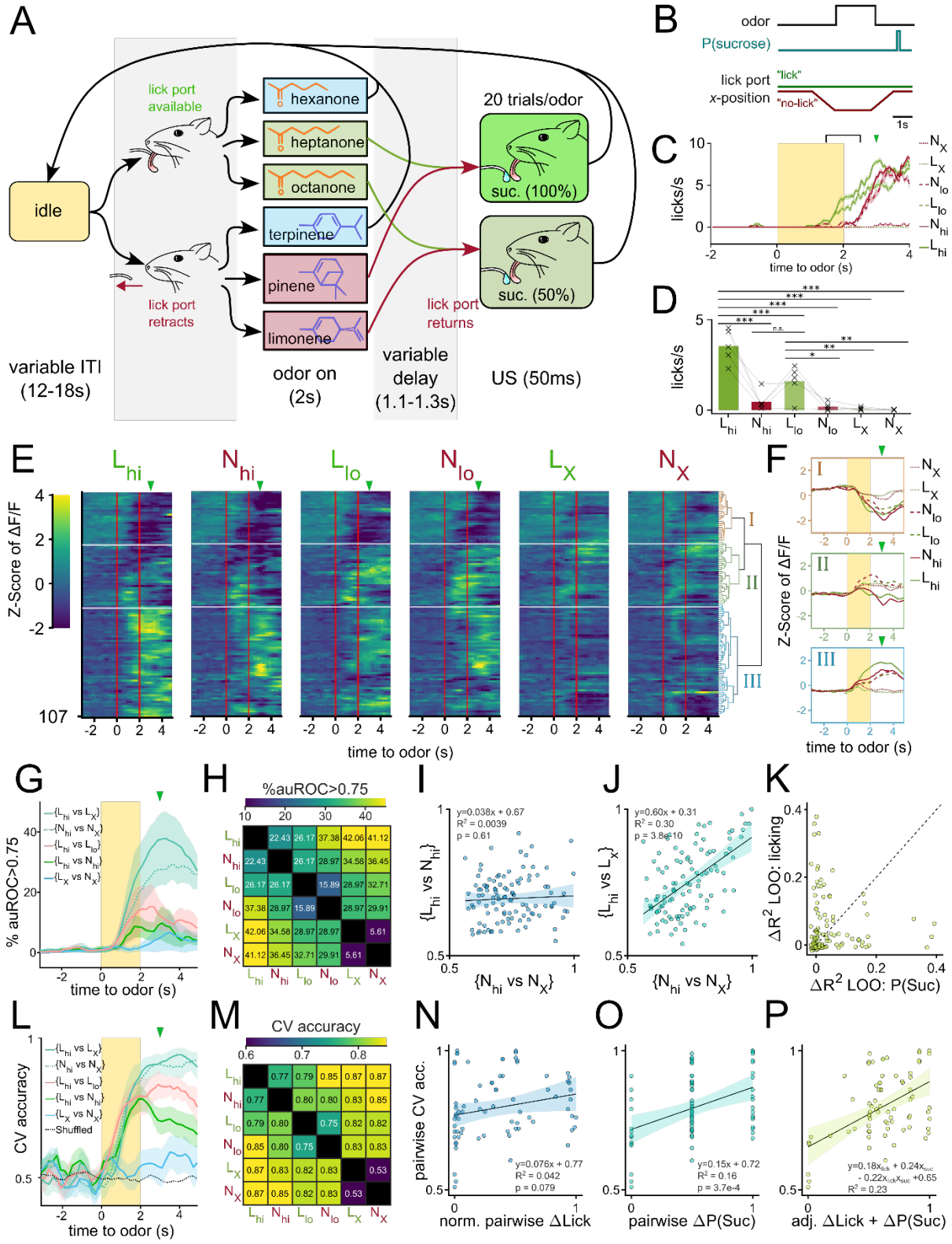
A
idle
lick port available
lick port retracts
hexanone
heptanone
octanone
terpinene
pinene
limonene
20 trials/odor
suc. (100%)
suc. (50%)
lick port returns
variable ITI (12-18s)
odor on (2s)
variable delay (1.1-1.3s)
US (50ms)
B
odor
P(sucrose)
lick port x-position
"lick"
"no-lick"
1s
C
licks/s
time to odor (s)
D
licks/s
E
Z-Score of ΔF/F
time to odor (s)
F
Z-Score of ΔF/F
time to odor (s)
G
% auROC>0.75
time to odor (s)
H
%auROC>0.75
I
y=0.038x + 0.67
R² = 0.0039
p = 0.61
J
y=0.60x + 0.31
R² = 0.30
p = 3.8e-10
K
ΔR² LOO: licking
ΔR² LOO: P(Suc)
L
CV accuracy
time to odor (s)
M
CV accuracy
N
pairwise CV acc.
y=0.076x + 0.77
R² = 0.042
p = 0.079
norm. pairwise ΔLick
O
y=0.15x + 0.72
R² = 0.16
p = 3.7e-4
pairwise ΔP(Suc)
P
y=0.18x_lick + 0.24x_suc - 0.22x_lick x_suc +0.65
R² = 0.23
adj. ΔLick + ΔP(Suc)

Figure 6. Separate VP populations encode reward-contingency and licking vigor. (**A**) State diagram for odor pairing paradigm where lick spout is removed during the presentation of half of the odors. The paradigm is similar to one described in Fig2A with the following key differences: 1) the lick spout is moved away from the animal's mouth during the presentation of half of the odors (N_{hi}, N_{lo}, N_X). 2) sucrose is delivered after a longer variable delay (1.1-1.3s). 3) 2 of the odors have 100% sucrose contingency (L_{hi}, N_{hi}), 2 of the odors have 50% sucrose contingency (L_{lo}, N_{lo}), and the other 2 have 0% sucrose contingency (L_X, N_X). (**B**) Schematic showing the timing of lick port movement relative to odor and sucrose delivery. (**C**) Licking behavior to 6 odors averaged across 30 trials from a representative animal. Duration of odor delivery is marked by the shaded rectangle and the average time of sucrose delivery is marked by the arrowhead. The time bin used for subsequent analysis (last 0.5s of odor and first 0.5s of delay) is outlined by square brackets (**D**) Average licks/s for each odor measured between the last 0.5s of odor and the first 0.5s of delay. Data were pooled from the day of highest difference between licks to L_{hi} and N_{hi}. (**E**) Heatmap of odor-evoked activity in VP neurons pooled from each animal's day of highest difference between licks to L_{hi} and N_{hi}. Neurons are grouped according to the clustering dendrogram, shown on the right. Horizontal white lines demarcate the boundaries between the 3 clusters. Odor delivery is marked by vertical red lines. (**F**) Average Z-scored activity of each cluster to each of the 6 odors. Yellow bar indicates 2-seconds of odor exposure. (**G**) The percentage of single-neuron linear classifiers with auROC>0.75 as a function of time relative to odor delivery. Shaded area represents the SEM across biological replicates (n=5). (**H**) Heatmap of the percentage of pooled VP neurons with auROC>0.75 during the last 0.5s of odor and first 0.5s of delay. (**I**) Scatterplot comparing the auROC for {L_{hi} vs N_{hi}} (y-axis) and {N_{hi} vs. N_X} (x-axis) for each neuron. The line of best fit is plotted as a dotted line, with the 95% confidence interval shaded in. (**J**) Same as (I) but comparing the auROC for {L_{hi} vs L_X} (y-axis) and {N_{hi} vs. N_X} (x-axis). (**K**) Scatterplot comparing regression models that explain each neuron's activity on a given trial as a function of anticipatory licking or sucrose contingency. The values plotted are the loss in R^2 in models without anticipatory licking (y-axis) or sucrose contingency (x-axis) when compared to a model with both variables and their interaction term. (**L**) CV accuracy for 5 different odor pairs as a function of time relative to odor delivery. (**M**) Heatmap of average pairwise CV accuracy trained on the last 0.5s of odor and the first 0.5s of delay. (**N**) Scatterplot of all pairwise classifier accuracies from all animals (y-axis) and the corresponding range-normalized average pairwise difference in anticipatory licking (x-axis). (**O**) Scatterplot of all pairwise classifier accuracies from all animals (y-axis) and the corresponding pairwise difference in reward-contingency (x-axis). (**P**) Scatterplot of all pairwise classifier accuracies (y-axis) and the adjusted combined model of ranged-normalized Δlick and Δreward-contingency (x-axis). FWER-adjusted statistical significance for post hoc comparisons are shown as: ***$p<0.001$, **$p<0.01$, *$p<0.05$, n.s. $p>0.05$. See Tables S30-31 for detailed statistics.